

University of Alberta

The Effect of Soft Tissue on the Propagation of Ultrasonic Guided Waves
Through Long Bones

by

Lauren Stieglitz

A thesis submitted to the Faculty of Graduate Studies and Research
in partial fulfillment of the requirements for the degree of

Master of Science

Department of Physics and Department of Biomedical Engineering

© Lauren Stieglitz
Fall 2011
Edmonton, Alberta

Permission is hereby granted to the University of Alberta Libraries to reproduce single copies of this thesis and to lend or sell such copies for private, scholarly or scientific research purposes only. Where the thesis is converted to, or otherwise made available in digital form, the University of Alberta will advise potential users of the thesis of these terms.

The author reserves all other publication and other rights in association with the copyright in the thesis and, except as herein before provided, neither the thesis nor any substantial portion thereof may be printed or otherwise reproduced in any material form whatsoever without the author's prior written permission.

Abstract

Guided waves have been successfully used to characterize long bone properties, however the layer of soft tissue covering bone must be considered for guided wave technology to be clinically viable. We analyzed the impact of soft tissue through *in vitro* experiments on a cortical bone plate with and without a soft tissue mimic, and *in vivo* experiments on human tibiae. Data was examined using time-frequency analysis and frequency-phase velocity spectra. The data exhibit consistently two distinctive wave packets of different velocities. Guided wave modes A_1 and S_1 are generated in the soft tissue-bone plate model in addition to A_0 and S_0 generated in the bone. The presence of soft tissue alters the guide wave energy distribution. Most of the guided wave energy is concentrate around 0.1 – 0.2 MHz. The same phenomenon was observed in the *in vivo* data. The *in vitro* experiments were in agreement with theoretical predictions.

Acknowledgement

I give my deepest gratitude to my supervisors Dr. Lawrence Le and Dr. Jeff Gu for all of their aid and guidance during my graduate work. Dr. Le in particular has always been very encouraging and given me invaluable help.

A number of people helped me on various aspects of this project. I would like to thank Dr. Mauricio Sacchi for his advice on the signal processing elements of this thesis, David Bonar for his assistance with the spectral decomposition, Alex Tsang for the data acquisition, Hongjiang Li for his help with the SVD and Ahmed Alhani for his assistance with the synthetic simulation. I also give my thanks to Dr. Dean Ta at Fudan University in China.

I thank the following institutions for their support Departments of Physics and Biomedical Engineering and NSERC.

Table of Contents

Chapter 1 Introduction.....	1
1.1 Bone Tissue.....	1
1.2 Osteoporosis	3
1.3 Radiation-based Osteoporosis Assessment.....	4
1.4 Ultrasound Assessment of Bone	6
1.5 Axial Transmission Method.....	8
1.6 Guided Waves	9
1.7 Soft Tissue Effects.....	14
1.8 Objectives and Outline.....	17
Chapter 2 Materials and Methods.....	21
2.1 <i>In Vitro</i> Experiment.....	21
2.2 <i>In Vivo</i> Experiment.....	24
2.3 Data Analysis	29
2.4 Waveform Simulation.....	33
2.5 Theoretical Dispersion Modeling	34
Chapter 3 Results.....	36
3.1 Bone Plate.....	36
3.2 Soft Tissue Bone Plate	39
3.3 <i>In Vivo</i> Human Tibia	42
Chapter 4 Discussion	74
4.1 Time Domain Data.....	74
4.2 Frequency Content.....	76
4.3 Numerical Simulation	80

4.4 Single Value Decomposition	81
4.5 Soft Tissue Complexities	84
4.6 Reliability and Repeatability.....	85
Chapter 5 Conclusion and Comments on Further Direction	88
Bibliography	90
Appendix A.....	98

List of Figures

Figure 1.1	A sketch of a long bone, with components labeled (taken from http://www.bbc.co.uk/schools/gcsebitesize/pe/appliedanatomy/2_anatomy_skeleton_rev4.shtml)	18
Figure 1.2	Comparison of normal bone and osteoporotic bone (taken from http://www.nlm.nih.gov/medlineplus/ency/imagepages/17156.htm).	18
Figure 1.3	Schematic diagram of an axial transmission experimental configuration	19
Figure 1.4	Guided wave propagation in a plate material. (From Joshi, 2006).	19
Figure 1.5	The shape of the A_0 and S_0 modes showing the deformation of the particles in a cross-sectional plane. The retrograde elliptical motion at the plate surface is also illustrated. (From Cheeke, 2002).	26
Figure 2.1	The bovine bone plate with the Aqualene TM elastomer couplant. Inset is an image showing the thickness of the bone plate	26
Figure 2.2	Experimental set-up for bone plate experiment. Water below the bone plate was used to mimic marrow	27
Figure 2.3	Experimental set up for the <i>in vivo</i> human tibia experiment	28
Figure 3.1	The $x - t$ diagram of the ultrasound signals for the BP. The records are self-normalized. The positive and negative values	

	represent the normalized amplitudes of the individual traces	46
Figure 3.2	The $x - t$ diagram of the ultrasound time signals for the BP. The image displays 20 out of 130 columns of the matrix in “wiggle” format. The records are self-normalized. Superimposed are the arrival times of the compressional wave (blue), shear wave (red), and Raleigh wave (green). The velocities of these arrivals are as follows: $v_{\text{compressional}} = 4000$ m/s, $v_{\text{shear}} = 1970$ m/s, and $v_{\text{Rayleigh}} = 1840$ m/s	47
Figure 3.3	The BP amplitude spectra at two offsets: (a) 40 mm and (b) 140 mm. The spectra are self-normalized	48
Figure 3.4	The $t - f$ plots for the BP at offsets 40 mm (a), 90 mm (b), and 140 mm (c). Also plotted is the time signal for (d) the bone plate at 140 mm offset	49
Figure 3.5	The $x - t$ diagram of the numerically simulated BP traces. The records are self-normalized.....	50
Figure 3.6	The $x - t$ diagram of the numerically simulated BP traces. The records are self-normalized. Superimposed are the arrival times of the compressional wave (blue), shear wave (red), and Raleigh wave (green).	51
Figure 3.7	Comparison of experimental (blue solid curve) and numerically simulated (red dashed curve) signals at 140 mm offset for the BP	52
Figure 3.8	The $f - c$ diagram for the BP data with theoretical dispersion curves (black solid lines) superimposed.....	52

Figure 3.9	Theoretical $f - c$ dispersion curves (black solid curves) for the BP data. Superimposed are the picked maximum intensity points from the experimental data (blue stars) and simulated data (red circles).....	53
Figure 3.10	The $x - t$ diagram of the ultrasound signals for the STBP. The records are self-normalized.....	54
Figure 3.11	The $x - t$ diagram of the ultrasound STBP traces. The records are self-normalized. Superimposed are the arrival times of the compressional head wave (blue), shear wave (red), and Raleigh wave (green); (The velocities of these arrivals are as follows: $v_{\text{compressional}} = 4000$ m/s, $v_{\text{shear}} = 1970$ m/s, and $v_{\text{Rayleigh}} = 1840$ m/s).....	55
Figure 3.12	The amplitude spectra for the STBP data at two offsets: (a) 40 mm and (b) 140 mm. The spectra are self-normalized.....	56
Figure 3.13	The $t - f$ plots for the STBP data at offsets 40 mm (a), 90 mm (b), and 140 mm (c). Also plotted is the time signal for (d) the STBP at 140 mm offset.....	57
Figure 3.14	The $x - t$ diagram of the numerically simulated STBP traces. The records are self-normalized	58
Figure 3.15	The $x - t$ diagram of the numerically simulated STBP traces. The records are self-normalized. Superimposed are the arrival times of the compressional wave (blue), shear wave (red), and Raleigh wave (green).	59

Figure 3.16	Comparison of experimental (blue solid curve) and numerically simulated (red dashed curve) traces at 140 mm offset for the STBP data.....	60
Figure 3.17	The $f - c$ diagram with theoretical dispersion curves (black solid lines) superimposed.....	60
Figure 3.18	Theoretical $f - c$ dispersion curves (black solid curves) for the STBP data. Superimposed are the picked maximum intensity points from the experimental data (blue stars) and simulated data (red circles).	61
Figure 3.19	The $x - t$ diagram of the ultrasound signals for the HT traces. The records are self-normalized.	62
Figure 3.20	The $x - t$ diagram of the ultrasound traces for the HT data. The records are self-normalized. Superimposed are the arrival times of the compressional head wave (blue), shear wave (red), and Raleigh wave (green).	63
Figure 3.21	The HT amplitude spectra at two offsets: (a) 40 mm and (b) 140 mm. The spectra are self-normalized.	64
Figure 3.22	The $t - f$ plots for the HT at offsets 40 mm (a), 90 mm (b), and 140 mm (c). Also plotted is the time signal for (d) the HT data at 140 mm offset.....	65
Figure 3.23	The $f - c$ diagram for the HT data.....	66
Figure 3.24	The $x - t$ diagram of the ultrasound signals for the HT SVD results. The records are self normalized	67

Figure 3.25	The amplitude spectra of the SVD HT data at two offsets: (a) 40 mm and (b) 140 mm. The spectra are self-normalized.....	68
Figure 3.26	The $t - f$ plots for the HT SVD data at offsets 40 mm (a), 90 mm (b), and 140 mm (c). Also plotted is the time signal for (d) the data at 140 mm offset	69
Figure 3.27	The $f - c$ diagram for the HT SVD results	70
Figure 3.28	The $x - t$ diagrams for (a) human tibia specimen 1 and (b) human tibia specimen 2	71
Figure 3.29	The frequency spectra for human tibia specimen 1 at (a) 40 mm, (b) 140 mm and human tibia specimen 2 at (c) 40 mm and (d) 140 mm offsets	72
Figure 3.30	The $f - c$ diagrams for human tibiae: (a) specimen 1 and (b) specimen 2	73

List of Abbreviations

BMD	Bone mineral density
SPA	Single photon absorptiometry
DPA	Double photon absorptiometry
DXA	Dual emission X-ray absorptiometry
BUA	Broadband ultrasound attenuation
FAS	First arriving signal
SOS	Speed of sound
FFT	Fast Fourier transform
2D	Two dimensional
BP	Bone plate
STBP	Soft tissue bone plate
HT	Human tibia

Chapter 1

Introduction

This thesis examines the effect of soft tissue on the propagation of ultrasonic guided waves through long bone. This research falls under the umbrella of ultrasound research on bone for the purpose of developing clinical means of evaluating bone quality with ultrasound. Clinical ultrasonic assessment methods have the potential to be used in the diagnosis and monitoring of osteoporosis.

1.1 Bone Tissue

Bone tissue is comprised of widely separated cells that are surrounded by a matrix of intercellular material. The matrix is made up of water (25%), collagen fibers (25%) and crystallized mineral salts (50%) (Tortora and Grabowski, 2003). The inorganic, crystallized mineral salts are mainly calcium phosphate and calcium carbonate. During bone formation, these minerals are deposited in a framework of collagen fibers that make up the bone matrix (Bilezikian, Raisz and Martin, 2008). This process is called calcification and only occurs in the presence of collagen fibers. The four types of cells present in bone tissue are osteogenic cells, osteoblasts, osteocytes and osteoclasts.

Bone tissue is porous and is characterized as either compact or spongy bone based on the size and distribution of the bone pores. These pores have many purposes including acting as channels for blood vessels or storage spaces for bone marrow. Compact bone is less porous and comprises approximately 80% of the skeleton while spongy bone is more porous and accounts for 20% of the skeleton.

Compact bone, or cortical bone, forms the protective external layer of all bones, the cortex. Compact bone provides skeletal support and resists mechanical stresses (Laugier and Haiat, 2010). Cortical bone makes up the shaft of long bones and resists fracture when large amounts of stress are applied (Fig. 1.1). Cortical bone is denser, harder and stronger than spongy bone; it also accounts for most of the skeleton's weight.

Spongy bone is made up of a lattice of thin spicules of bone called trabeculae; it is consequently referred to as trabecular bone. The pore spaces in spongy bone hold red bone marrow; the trabeculae both protect and support the marrow. As it is considerably lighter than cortical bone, spongy bone serves to reduce the overall weight of a bone, which increases mobility (Fig. 1.1).

These two types of bone tissue make up the four types of bones: short bones (carpals, tarsals), flat bones (cranium, ribs), irregular bones (vertebrae) and long bones (femur, humerus). Short bones are nearly equal in length and width and are comprised mostly of spongy bone. Flat bones are made of two parallel layers of cortical bone enclosing a spongy layer and are generally quite thin. Irregular bones have more complex shapes and cannot be classified as any other type of bone. Long bones, which this

study focuses on, are longer than they are wide (Tortora and Grabowski, 2003). The cylindrical shaft of long bone, the diaphysis, is made of compact bone surrounding the medullary, or marrow, cavity. Spongy bone forms the epiphysis (the ends) of long bone and lines the medullary cavity.

1.2 Osteoporosis

Osteoporosis is a metabolic bone disease characterized by low bone mass and deterioration of bone micro-architecture resulting in changes to the mechanical properties of bone (Werner, 2004). Osteoporosis is also defined as a condition of generalized skeletal fragility (Marcus, 2008), leading to increased fracture risk. In osteoporosis, there is an imbalance between bone formation and bone resorption. This is largely caused by the depletion of calcium in the body, where more calcium is lost than is absorbed from one's diet. Osteoporosis decreases the strength of bone in multiple ways. In cortical bone, resorption leads to thinning of the dense, outer cortical bone layer (Turner, 2002; Moilanen et al., 2007a). In cancellous bone, trabeculae weaken and break, decreasing the strength and connectivity of bone micro-architecture (Bartl and Frisch, 2009) (Fig. 1.2). These major factors lead to decreased bone quality and an increased risk of fracture.

Osteoporosis affects over 200 million people worldwide (Reginster and Burlet, 2006) including two million Canadians (Grampp and Adams, 2008). Approximately 1 in 4 women and 1 in 8 men over the age of 50 have osteoporosis (Grampp and Adams, 2008; Brown and Josse, 2002).

The estimated cost of osteoporosis to the Canadian healthcare system is \$1.9 billion a year (Osteoporosis Canada, 2011). Osteoporosis presents a serious health risk; it greatly increases the risk of fractures in the elderly, accounting for 80% of fractures in people over 60 (Osteoporosis Canada, 2008). Adding to its cost, osteoporosis accounts for more hospital bed days than stroke, heart attack or diabetes. Each year, over 70% of Canada's 30,000 hip fractures are attributed to osteoporosis; hip fractures cost a minimum of \$20,000 each and lead to death in up to 30% of cases. This silent epidemic is often asymptomatic until a fracture occurs (Werner, 2004; Njeh, Boivin and Langton, 1997), making monitoring and early detection of osteoporosis important for the prevention of fractures.

1.3 Radiation-based Osteoporosis Assessment

The most common way to assess and diagnose osteoporosis is bone mineral density (BMD) testing. BMD tests determine the density of calcium hydroxyapatite, or bone mineral, at a test area using photon absorptiometry techniques. Photon absorptiometry methods depend on measuring the attenuation of photons or X-rays through bone material (Bonnick, 2010) and include single-photon absorptiometry (SPA), double-photon absorptiometry (DPA) and dual emission X-ray absorptiometry (DXA). SPA and DPA use a radioactive isotope as the photon source with one and two photoelectric peaks, respectively. Those methods are limited by the disposal and replacement of the radionuclide source, long acquisition times and poor image quality caused by a limited amount of

photons produced. The most commonly used and widely available BMD test is DXA, which uses X-rays as the photon source. DXA measures BMD at a specific location, such as the hip, based on differential attenuation of two X-ray beams with different energies (Adler, 2010). The differential energy beams allow DXA to measure both the areal density of the bone and soft tissue components, making it possible to isolate the BMD.

The main risk of DXA testing is the use of ionizing radiation. The dose of a typical DXA test is fairly low, approximately the same as a few days' worth of background radiation (Adler, 2010). However, with repeated BMD tests, a patient's dose will accumulate. Additionally, there are multiple sources of error in DXA measurements. DXA is dependent on bone size; a larger-sized or thicker bone will always be found to have a larger BMD (Adler, 2010). BMD tests are also dependent on fat distribution as the BMD calculation assumes only two components in human tissue: bone and soft tissue. Beam hardening is another factor that reduces accuracy. Beam hardening is a phenomenon where the BMD measurement depends on the total thickness of tissue (bone and soft tissue) traversed by the beam. Radiation sources are not monochromatic and contain a distribution of X-ray energies; as an X-ray beam travels through the body, the lower energy photons are preferentially absorbed. The average energy of the beam becomes higher or "hardens." In a large body, beam hardening is more pronounced, resulting in a different BMD measurement.

1.4 Ultrasound Assessment of Bone

In recent decades, quantitative ultrasound has been proposed to assess bone as an alternative to radiation-based technologies. Research in ultrasound assessment of bone has been ongoing for the last forty years. Early use of ultrasound in the study of bone focused on the monitoring of fracture healing. Ultrasound gained renewed interest in 1984, when the measurement of broadband ultrasonic attenuation (BUA) was described by Langton et al. (1984) for the assessment of bone quality.

There are many benefits to the use of ultrasound. It is cost effective, portable, easy to use and does not involve the ionizing radiation present in X-ray-based technologies. The latter is important, as the clinical use of ultrasound will reduce patient radiation dose. Though X-ray absorptiometry is successful in measuring bone mineral density, it cannot determine other important measures of bone strength, such as bone microstructures and elasticity (Laugier, 2006; Moilanen, 2008). Ultrasound involves the propagation of mechanical waves through a medium, so it is affected by the mechanical and physical properties of the transmitting medium, including cortical thickness, micro-architecture, density, elasticity and porosity (Muller et al., 2005). These properties are important in the assessment of bone status for osteoporosis risk.

Transverse Transmission Method

The transverse transmission method was proposed by Langton et al. (1984) for the clinical diagnosis of osteoporosis. This method measures

BUA by transmitting ultrasound from a transducer to a receiver on the opposite side of the object of study. Their study focused on the calcaneus, or heel bone, as it is approximately 90% cancellous bone (Langton and Njeh, 2008). The attenuation of ultrasound in bone was found to be proportional to the frequency. This frequency dependence is different between osteoporotic bone and healthy bone, indicating that this technique could be used to evaluate bone quality. Many subsequent studies have examined BUA at the heel bone, resulting in a series of clinical ultrasound bone measurement systems (Njeh, Boivin and Langton, 1997). Studies have investigated the relationship between BUA and bone density and found high correlations between BUA and apparent density (Verhoef, Cloostermans and Thijssen, 1985). Further, Han et al. (1996) found correlations between BMD and BUA or ultrasound velocity. Duquette et al. (1997) examined which bone components BUA was influenced by; they concluded that BUA is sensitive to bone mineral content and unaffected by the presence of the organic matrix.

There are also many potential sources of error in BUA measurements including interface losses, diffraction and phase cancellation (Langton and Njeh, 2008). Diffraction errors are considered to be negligible when the sample is immersed (Verhoef, Cloostermans and Thijssen, 1985). However, in the contact method, the transducers are placed directly on the sample and the transducer separation changes to accommodate heel or sample thickness which can create significant diffraction errors (Langton and Njeh, 2008). Interface losses become an issue when a heel or intact calcaneus are studied, accounting for up to 20

dB of additional attenuation. (Langton and Njeh, 2008). Langton and Njeh (2008) also found that the ability of BUA to determine the mechanical properties of bone decreased in *in vivo* studies in comparison to *in vitro* studies involving cubes of cancellous bone (Langton and Njeh, 2008).

1.5 Axial Transmission Method

The axial transmission method measures the mechanical properties of long bone along the shaft of the bone sample (Moilanen, 2008; Lowet and Perre, 1996; Bossy, Talmant and Laugier, 2004; Tatarinov, Sarvazyan and Sarvazyan, 2005; Ta et al., 2009; Le et al., 2010). Specially designed for cortical bone assessment, this technique was first developed over forty years ago for fracture monitoring (Siegel, Anast and Fields, 1958; Gerlanc et al., 1975). In those studies, the results were used to measure the velocity of ultrasound waves across a fracture during the healing process.

For the experimental setup, the transmitting and receiving transducers are deployed rectilinearly on the same side of the bone sample. During data acquisition, the transmitter is stationary and the receiver is moved away from it at a fixed increment (Fig. 1.3). Time signals are obtained at each transmitter-receiver distance or offset.

In this configuration, the ultrasound signal travels along the long axis of the bone from the transmitter to the receiver. At small source-receiver offsets, strong body waves are observed (Le et al., 2010). At far source-receiver offsets, energetic guided wave modes are also generated

(Lefebvre et al., 2002; Nicholson et al., 2002; Moilanen et al., 2006). Depending on whether there is a soft tissue layer overlying the cortex, a direct wave or a lateral wave (head wave) will be generated as the first arriving signal. This lateral wave was studied by Camus et al. (2000). The travelling velocity, or speed of sound (SOS), of the FAS has also been shown to correlate to bone properties (Bossy et al., 2004). The velocity of the FAS is dependent on cortical thickness (Njeh et al., 1999; Bossy, Talmant and Laugier, 2002). Moilanen et al. (2004) found that the low frequency velocity measurements were sensitive to local cortical thickness, while high frequency measurements were not. Additionally, it has been observed that axial transmission SOS measurements are sensitive to intracortical porosity tissue mineralization (Bossy et al., 2004). Sievänen et al. (2001) found that cortical density was a strong determinant of the SOS in tibia and radial cortexes; they suggested that the material properties of bone strength were related to the bone density, and in turn were associated with the SOS. Prevrhal et al. (2001) found that the SOS measurement depends on both cortical thickness and the density of the tibia.

1.6 Guided Waves

In recent years, ultrasound guided waves have generated considerable interest for their sensitivity to bone properties. Guided waves have been widely used in non-destructive testing to characterize material properties (Chimenti, 1997). In industry, guided waves are used to detect

material defects and fractures in such diverse structures as pipelines and airplane fuselages (Joshi, 2006).

Guided waves are generated by the interference and superposition of reflected or mode-converted longitudinal and shear body waves within a layer bounded by strong reflectors (Viktorov, 1967; Rose, 1999). Longitudinal and shear waves entering a plate from a transducer will be reflected and mode converted at boundaries with an impedance contrast; the multiple reflections of the signals will superimpose over a distance to generate guided waves (Fig. 1.4).

Guided waves propagating in plates are referred to as Lamb waves and are dispersive, meaning that the propagating velocities depend on frequency. Lamb waves are dispersive for finite values of the ratio of the wavelength (λ) to plate thickness (b). Determination of the dispersion relation of Lamb waves is useful in the study of bone.

Though long bone is roughly cylindrical, it has been shown that guided waves in bone can be successfully modeled with Lamb waves (Lefebvre et al., 2002; Protopappas, Fotiadis and Malizos, 2006). Lefebvre et al. (2002) used Lamb wave theory to accurately predict phase velocities for ox bone. Good comparisons between theory and experiments have been demonstrated for metal plates (Minonzio, Talmant and Laugier, 2010), acrylic plates (Lee and Yoon, 2004), and cortical bone plates (Bossy, Talmant and Laugier, 2002). Bossy, Talmant and Laugier (2004) found that two dimensional (2D) plate models were effectively equivalent to cylindrical models for phase velocity measurements. The first longitudinal and flexural modes in a cylinder are very similar to the fundamental anti-

symmetric and symmetric modes in plates of the same thickness (Lefebvre et al., 2002; Cheeke, 2002). Modeling bones as plates, as a first order approximation, is accurate enough to give useful information about the mechanical properties of bone.

Lamb waves in a plate are described by the following dispersion equation:

$$\frac{\tan(\beta d / 2)}{\tan(\alpha d / 2)} = \left\{ -\frac{4\alpha\beta k^2}{(k^2 - \beta^2)^2} \right\}^{\pm 1}, \quad (1)$$

$$\alpha^2 = \frac{\omega^2}{c_L^2} - k^2, \text{ and} \quad (2)$$

$$\beta^2 = \frac{\omega^2}{c_T^2} - k^2 \quad (3)$$

where d is plate thickness, k is wavenumber, ω is angular frequency, c_L is longitudinal velocity in the solid, and c_T is transverse velocity. The derivation of these equations is outlined in Appendix 1.

Lamb waves travel in modes where each mode represents a solution to equation (1), in other words, each mode represents a form of the propagating wave. This equation can only be solved numerically and is used to determine the phase velocity of a wave propagating at a specific frequency in a plate; it is referred to as a dispersion relation. Lamb wave modes are defined by their particle motion as either symmetric or anti-symmetric. In equation (1), the exponent “+1” represents the symmetric modes and the “-1” for anti-symmetric modes. Symmetric modes, identified as S_0 , S_1 , S_2 , etc, have particle motion that is symmetric about the mid-plane of the plate, along the propagation direction. The anti-symmetric modes (A_0 , A_1 , A_2 , etc) have particle motion that is anti-symmetric along

the propagation direction. The fundamental symmetric S_0 and anti-symmetric A_0 modes are the lowest frequency modes and exist at all frequencies while higher order modes have a cut-off frequency under which they do not propagate (Cheeke, 2002). Each higher order mode begins to propagate above a specific resonant frequency of the plate and is only present above that frequency. The shapes of the two fundamental modes are illustrated in Figure 1.5.

Lamb waves are very similar to Rayleigh waves, the difference being that Lamb waves have a finite length scale, the plate thickness. When the wavelength approaches the plate thickness, the wave behaves like a Lamb wave. In the case of a Lamb wave traveling in a thick plate, it will begin to act like a Rayleigh wave. Additionally, as frequency increases, the velocities of Lamb modes tend towards the Rayleigh wave velocity (Nicholson et al., 2002). Mathematically, the same set of partial differential equations governs the wave propagation; it is the boundary conditions that set them apart.

As guided waves are created by multiple reflections and wave interference within a material, guided waves are capable of travelling longer distances than body waves. In bone, this means that guided waves interact with a larger portion of the bone sample. Guided waves travel in multiple modes, each with a phase velocity dependent on frequency. These modes are sensitive to the boundaries, thickness and structure of bone (Rose, 1999; Lee and Yoon, 2004; Vavva et al., 2008). The sensitivity of guided waves to cortical thickness is of particular interest as cortical thinning is an indicator of osteoporosis. While the task of identifying and

analyzing guided wave modes is challenging, they are worth studying as their multi-mode and dispersive characteristics provide important information about bone properties (Moilanen et al., 2006; Ta et al., 2006).

A variety of experiments have examined the sensitivity of guided waves to bone properties (see Moilanen (2008) for a comprehensive overview); the following outlines a few significant studies. Nicholson et al. (2002) examined the tibia of eight healthy and eight osteoporotic patients. They found that the velocity of a Lamb-type wave was, on average, 15% lower in osteoporotic patients than in the healthy group. Lefebvre et al. (2002) demonstrated that guided waves could determine the Young's modulus of bone; they used pulse-echo measurements of Lamb waves to estimate the Young's modulus and found that results agreed with those in literature. Guided wave propagation greatly depends on the thickness of the material it propagates in (Joshi, 2006) and the same has been observed in bone studies. The A_0 mode has been shown to be very sensitive to thickness (Tatarinov, Sarvazyan and Sarvazyan, 2005; Lefebvre et al., 2002). Moilanen et al. (2007b) developed a 2D numerical bone model and performed an inversion on their simulated data to estimate cortical thickness. They found that, though the model was simplistic, the simulated data was consistent with the *in vitro* bone data. Additionally, it was observed by Protopappas et al. (2007) that irregular bone geometry affected the dispersion of higher order guided wave modes.

Furthermore, multiple studies have determined that low frequencies are optimal for the study of guided wave propagation. Lee and Yoon (2004) were able to excite anti-symmetric and symmetric guided wave

modes. They found that the two most dominant modes, A_0 and S_0 , were present at low frequencies and determined that 0.2 MHz was the optimal frequency to study guided waves. Muller (2004) also found low frequencies are ideal.

Various data imaging and signal processing techniques have been used to analyze guided waves and extract useful information. These methods include spectral analysis (Vavva et al., 2008), 2D fast Fourier transform (FFT) (Alleyne and Cawley, 1991), singular value decomposition (SVD) (Minonzio, Talmant and Laugier, 2010) and time-frequency ($t - f$) analysis (Prosser, Seale and Smith, 1999).

1.7 Soft Tissue Effects

Soft tissue presents a significant challenge in the study of guided waves in bone. As guided waves travel through a bone covered in soft tissue, the guided waves interact with the cortical boundaries of the bone (Moilanen, 2008). Therefore, the soft tissue-bone interface affects the propagation of guided waves. When a plate is surrounded by a liquid or soft tissue, guided wave energy can “leak” out of the waveguide as they propagate (Lee and Yoon, 2004); for this reason Lamb waves in an immersed plate can be referred to as Leaky Lamb waves. In order for clinical applications of guided wave study in bone to be feasible, the affect of soft tissue on ultrasound transmission needs to be taken into account.

This presents a few challenges. First, soft tissue alters guided wave mode generation and changes the dispersive characteristics of modes,

affecting the consistency of mode identification (Moilanen, 2008). Second, the propagation velocity of soft tissue (1400 m/s - 1600 m/s) is in the range of guided wave velocity in bone (1300 m/s - 2000 m/s). As these signals arrive in the same time range, the signals from the soft tissue body wave have the potential to be mistaken for guided waves in bone (Moilanen et al., 2006). Lastly, soft tissue attenuates the incident ultrasound pulse, thus decreasing the signal-to-noise ratio of the data (Lee and Yoon, 2004).

Guided wave interaction with tissue is not well understood and this topic has not yet been sufficiently examined. Existing studies have generally focused on either numerical modeling (Vavva et al., 2008; Moilanen et al., 2008) or on modeling soft tissue by immersing bones and phantoms in water (Lowet and Perre, 1996; Lee and Yoon, 2004). In the latter case, soft tissue over bone is treated as a fluid-solid bi-layer where water is used to simulate soft tissue. Soft tissue has similar mechanical properties to water so it is commonly used as a soft tissue proxy (Culjat et al., 2010).

Early studies examined on how soft tissue affected transit times and velocity measurements in cortical bone. Lowet and Perre (1996) showed that a soft tissue layer of constant thickness and velocity produces a constant lag in the transmission time of a lateral wave travelling through the cortical layer. This lag can be removed to calculate the velocity of the FAS signal in bone. However, soft tissue is not uniform or homogenous. For a soft tissue layer on non-uniform thickness, Bossy et al. (2004) used a

bidirectional axial transmission approach to compensate for soft tissue effects in cortical bone velocity measurements.

Dodd et al. (2006) examined the effect of fluid loading on guided wave transmission through a plate. They studied five acrylic plates of varying thickness and also performed a 2D numerical simulation for cortical and acrylic plates. Their results showed that, in the acrylic plates, the S_0 and S_1 dispersion curves are significantly changed. In the cortical plates, the S_1 mode was changed while S_0 only had a small deviation from the unloaded curves. To model the effect of soft tissue, Moilanen et al. (2006) measured guided waves in free and immersed aluminum and acrylic plates using water as a soft tissue mimic. They identified the A_0 mode in the free plate and, in the immersed model, bi-layer modes. It was noted that in the immersed case, mode identification was difficult. They were able to determine plate thickness using an inversion scheme. Moilanen et al. (2008) used a fluid-solid bi-layer tube model to mimic soft tissue on a roughly cylindrical bone; this model was used to interpret *in vivo* data. This study examined how the thickness of the soft tissue layer affects guided waves, finding that mode identification and interpretation was difficult for thicker soft tissue layers. They also found that for increasing thicknesses of soft tissue, guided wave dispersion curves were more densely packed together.

Fluids cannot support shear stresses, so modeling soft tissue with a fluid-solid bi-layer may not fully explain the effect of the soft tissue-bone interface or the propagation and dispersion of guided wave modes. Nevertheless, previous investigations have provided valuable contributions

to the understanding of *in vivo* guided wave measurements. Currently, the impact of soft tissue on guided wave propagation in long bone has not been sufficiently explored. Guided wave measurements have great potential to play an important role in characterizing cortical bones. The effect of overlying tissue upon guided wave mechanics in long bones must be studied to provide guidance and confidence in analyzing *in vivo* data.

1.8 Objectives and Outline

The objective of this thesis is to examine the effect of soft tissue on guided wave propagation by means of experimental work and numerical modeling. The motivation of this study comes from an *in-vivo* experiment where the existence of strong guided waves is observed in human tibiae. In order to fully understand the *in vivo* data, we investigated the effect of soft tissue on the propagation of guided waves in a cortical bone plate. Chapter 1 provides background information about the topic. This chapter includes descriptions of osteoporosis, radiation-based bone assessment methods, ultrasound methodology and an introduction to guided waves and the challenges presented by the presence of soft tissue. Chapter 2 outlines the experimental procedures for the *in vitro* bone plate experiments and the *in vivo* experiment. Results and data analysis are presented in Chapter 3. Chapter 4 discusses the experimental data. A brief discussion of future direction concludes this thesis in Chapter 5.

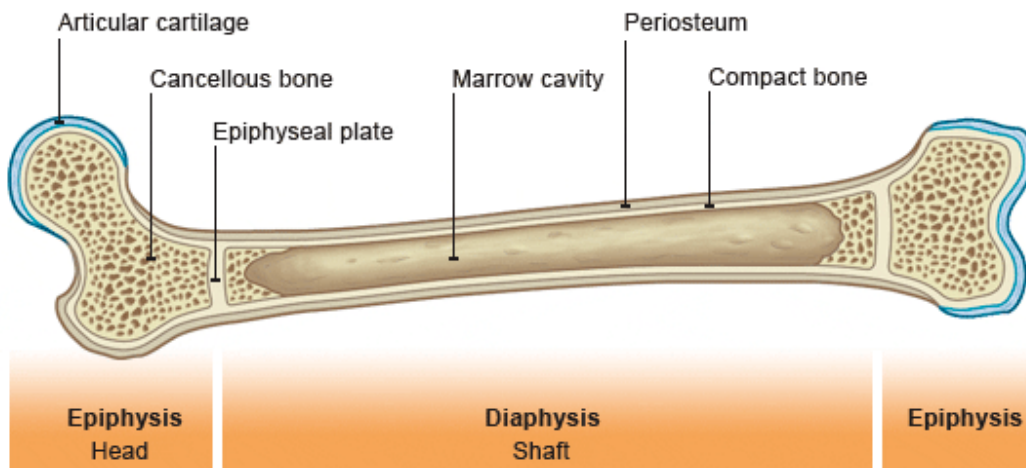


Figure 1.1 A sketch of a long bone, with components labeled (taken from http://www.bbc.co.uk/schools/gcsebitesize/pe/appliedanatomy/2_anatomy_skeleton_rev4.shtml).

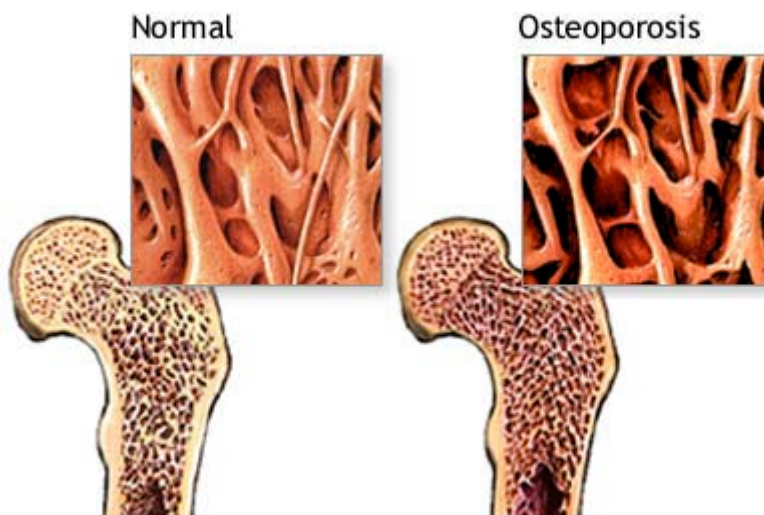


Figure 1.2 Comparison of normal bone and osteoporotic bone (taken from <http://www.nlm.nih.gov/medlineplus/ency/imagepages/17156.htm>).

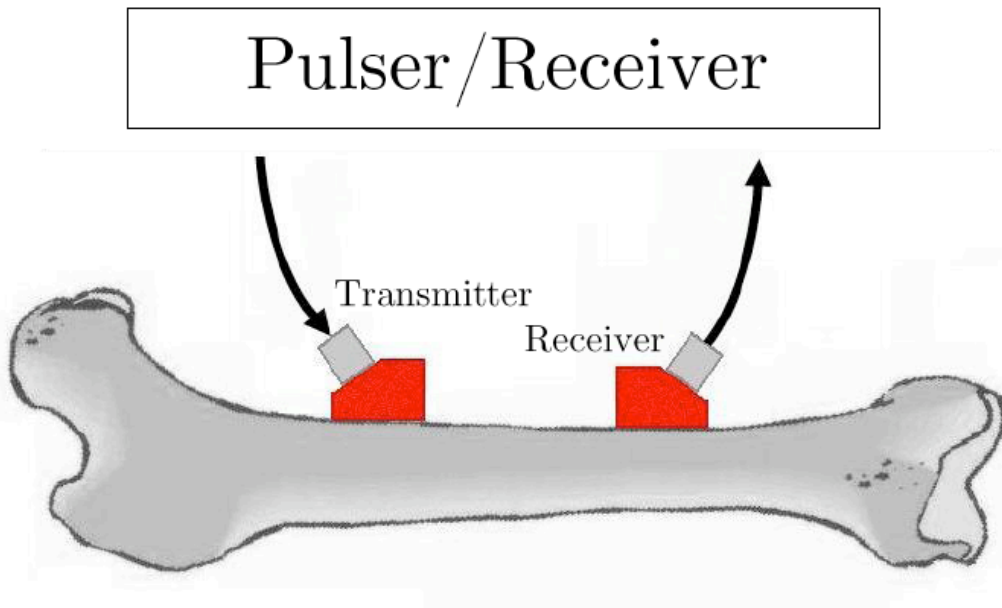


Figure 1.3 Schematic diagram of an axial transmission experimental configuration.

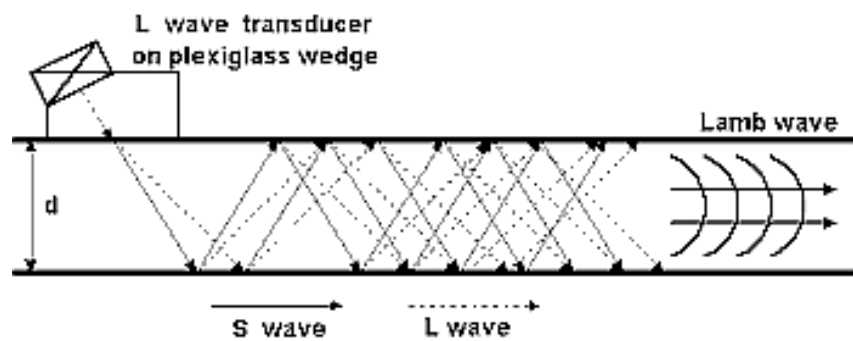


Figure 1.4 Guided wave propagation in a plate material. (From Joshi, 2006).

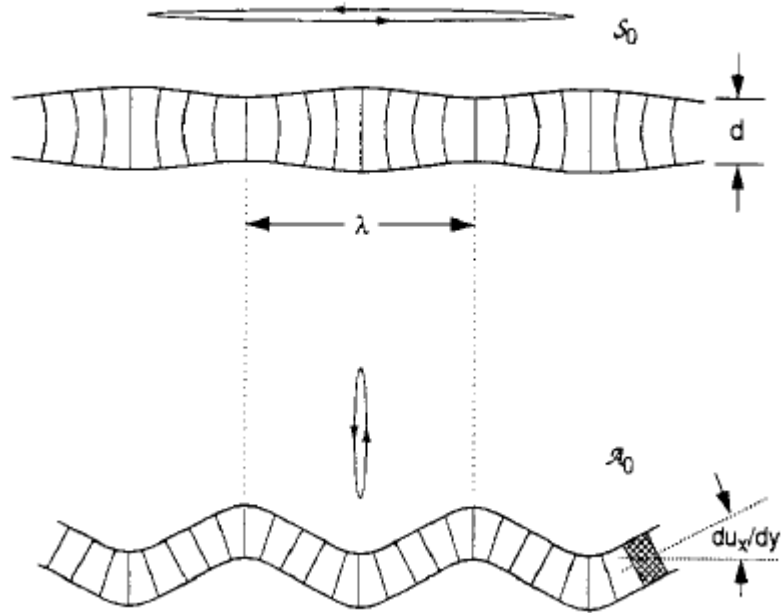


Figure 1.5 The shape of the A_0 and S_0 modes showing the deformation of the particles in a cross-sectional plane. The retrograde elliptical motion at the plate surface is also illustrated. (From Cheeke, 2002).

Chapter 2

Materials and Methods

2.1 *In Vitro* Experiment

We obtained a fresh bovine femur from a local butcher shop. The marrow and the soft tissue overlying the bone were removed. The ends of femur were removed with a band-saw, reserving the diaphysis mid-shaft portion. To make the bone plate, the bone was cut along the long axis, and the flat, top portion of cortical bone was retained. The bone plate was cleaned to remove all residual soft tissue and marrow. The cortical plate has dimensions of 230 mm (length) by 50 mm (approximate width) by 9 mm (mean thickness).

To model soft tissue, this study used an Olympus AqualeneTM elastomer couplant (Olympus NDT Inc., Waltham, MA). The dimensions of the couplant are 203 mm (length) by 102 mm (width) and 2.5 mm (thickness). The AqualeneTM material has similar properties to soft tissue (including skin) and supports shear wave propagation. This material has a low attenuation coefficient (0.28 dB/mm at 5 MHz); assuming a linear relationship between attenuation and frequency, this translates to an attenuation of 0.56 dB/cm MHz, which is comparable to the attenuation of soft tissue (0.54 dB/cm MHz) (Culjat et al., 2010). The shear wave velocity in AqualeneTM is 800 m/s and the compressional wave velocity is

1590 m/s. To compare, the average compressional velocity in soft tissue is 1561 m/s (Culjat et al., 2010). Figure 2.1 shows the bone plate with the soft tissue mimic. Inset is the side view of the bone plate.

We modeled marrow with water. Water has a compressional velocity comparable to marrow ($v_{\text{water}} = 1480$ m/s versus $v_{\text{marrow}} = 1435$ m/s) and is commonly used as a marrow mimic (Culjat et al., 2010).

Experimental Procedure

Two *in vitro* experiments were performed on the bone plate, one without the soft tissue (denoted as BP for bone plate) and one with the soft tissue mimic (denoted as STBP for soft tissue bone plate).

In the BP experiment, the bone plate was placed on top of two rubber stoppers in a small water tank. The water level reached just below the top of the bone so that the bone was not submerged; care was taken to ensure that no air bubbles were trapped under the bottom surface of the bone plate. Experimental measurements were performed at a room temperature of 21°C. The experiments used two angle beam compressional wave transducers as the source and receiver, each with a central frequency of 1 MHz (Panametrics C548, Waltham, MA). The diameter of the transducer is 1.3 cm. These were attached to two angle wedges (Panametrics ABWM-7T-30 deg) that formed incident and receiving angles of 24.4°¹. One transducer acted as the stationary source and the

¹ Calculated using Snell's law ($\sin\vartheta_1/v_1 = \sin\vartheta_2/v_2$). The 30° angle refers to the angle of transmission of a shear wave into steel ($v_{\text{shear}} = 3240$

other acted as the receiver. The transducer-wedge system was deployed linearly on the top surface of the bone plate (Fig. 2.2) in an axial transmission configuration. Ultrasound gel was used to ensure good coupling between the bone plate and the transducer wedges. Two steel bars were pressed against the bone plate, providing constant pressure to the transducer-wedge system so that contact was maintained. The transmitter was powered by a Panametrics 5800 Pulser/Receiver. The indecent signal is a broadband pulse. The resultant signal was collected by the receiver then digitized by and displayed on a 200-MHz digital storage oscilloscope (LeCroy 422 WaveSurfer, Chestnut Ridge, NY). The transducers started at a source-receiver distance or offset of 35 mm. The receiver was moved away from the transmitter at an increment of 1 mm to a final offset of 165 mm. This made for a total of 130 ultrasound time series' or traces.

In the STBP experiment, the AqualeneTM couplant was placed on top of the bone. Ultrasound gel was used to ensure good coupling and care was taken to make sure that there was no trapped air under the soft tissue proxy. The same procedure followed for the BP model, described above, was repeated here. A total of 130 traces were obtained.

During acquisition for both data sets, the traces were internally averaged 128 times. This was done to increase the signal-to-noise ratio and ensure that the received signals were in phase. In MATLAB, the recorded

m/s). Using the compressional velocity in the wedge ($v_{\text{compressional}} = 2680$ m/s), the incident angle is calculated.

data was decimated to 3985 time samples so that the results have a sampling interval of 0.05 μ s. The ultrasound data was stored in a distance-time ($x - t$) matrix of amplitudes, where each recorded trace represents a column of the matrix.

Signal Processing

The raw data for both cases included a late-arriving, large-amplitude signal generated by the reflection of the ultrasound waves off the bottom of the water container. This signal did not interfere with the bone plate data, so it could be easily removed. Using MATLAB, this reflection was eliminated through windowing, where the signal outside of a chosen window is muted.

The data was band-pass filtered to remove high-frequency noise. The band-pass window was 0.001 MHz/0.01 MHz/0.8 MHz/1.2 MHz. The data was debiased by zero-averaging the traces. For visualization purposes, the data was self-normalized.

2.2 *In Vivo* Experiment

The *in vivo* experiment was performed on the tibiae of two volunteers using the axial transmission technique. The first experiment was denoted as HT (HT stands for human tibia). The same 1 MHz transducer-wedge configuration and Pulser/Receiver used in the *in vitro* plate experiments was used here. During acquisition, subject's right leg was rested horizontally on a chair (Fig. 2.3). Two flexible rulers were laid

out on the flat part of the tibia and secured with medical tape to create a guide for the transducer wedges. The transducer-wedge system was laid out on the tibia in the axial transmission configuration. Ultrasound gel was used to ensure good coupling between the skin tissue and the transducer wedges. The experiment was performed at a room temperature of 21°C. The stationary source transducer was placed below the knee and held in place with tape. The receiving transducer was moved by hand at an increment of 2 mm. Each record was averaged 128 times during acquisition to increase the signal-to-noise ratio and decimated to 3500 samples with a sampling interval of 0.04 μ s. The initial offset was 30 mm, and the final offset was 170 mm for a total of 71 traces.

A second human tibia experiment was performed on another subject (denoted as HT2) to determine whether the *in vivo* results could be repeated, and this data will be discussed in that context only. The HT2 experiment followed the same procedure as the HT experiment.

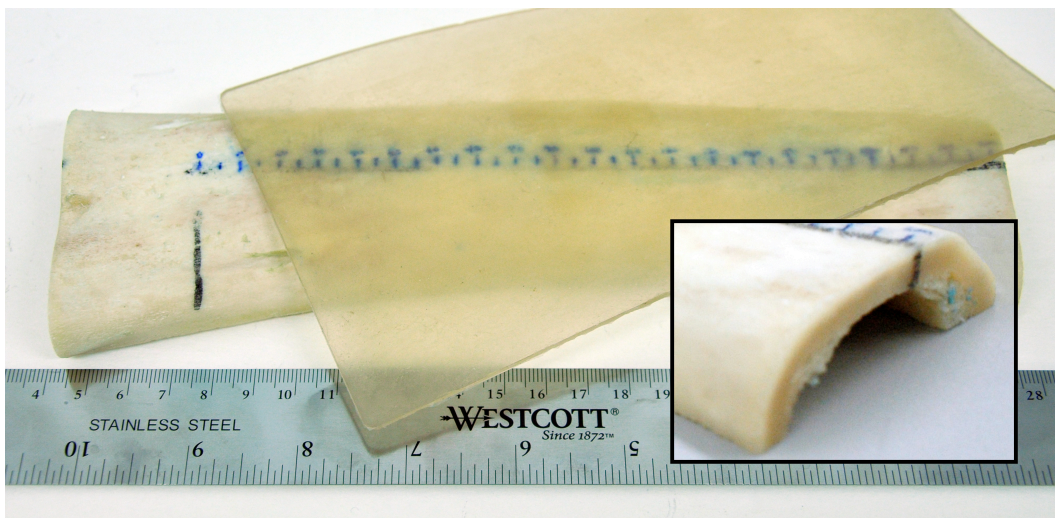


Figure 2.1 The bovine bone plate with the Aqualene™ elastomer couplant. Inset is an image showing the thickness of the bone plate.

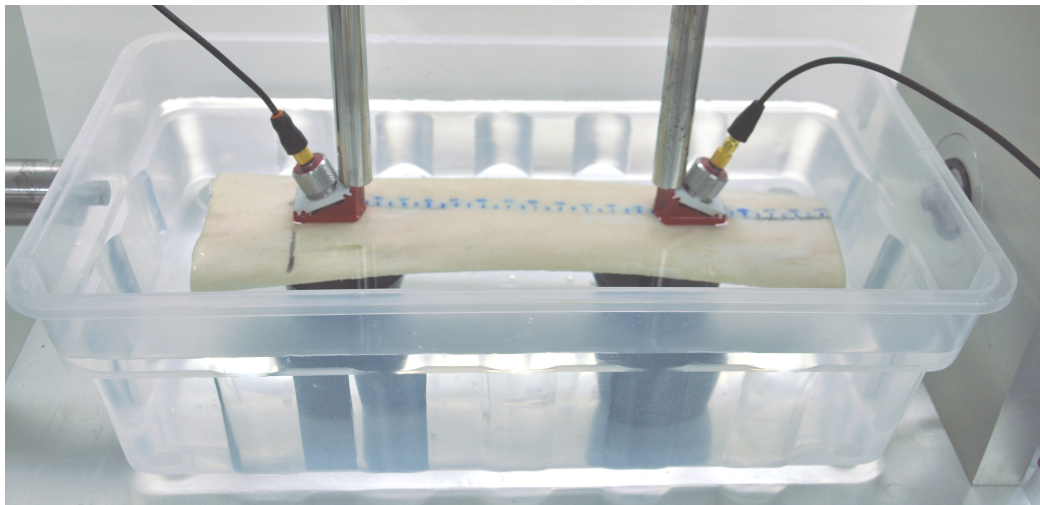


Figure 2.2 Experimental set-up for bone plate experiment. Water below the bone plate was used to mimic marrow.

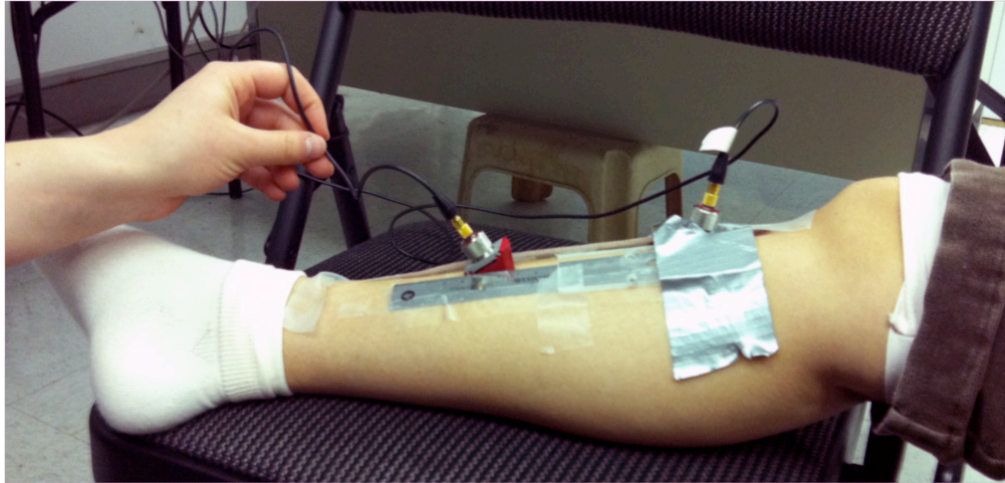


Figure 2.3 Experimental set up for the *in vivo* human tibia experiment.

Signal Processing

The human tibia data set was greatly attenuated and had a low signal-to-noise ratio, so more vigorous signal processing was needed. In the late time portion of the data, there was a strong signal that arrived after the guided and body waves. This signal was muted out with windowing in order to focus on the guided and body waves in the data.

The data was interpolated in MATLAB with a first-order $f - x$ interpolation using Spitz's method (Spitz, 1991). The interpolation code was provided by Dr. Mauricio Sacchi of the Signal Analysis and Imaging Group at the University of Alberta. This method is based upon the idea that linear events equally spaced in a data section may be interpolated exactly. In the $f - x$ domain, linear events are predictable, allowing for

missing traces to be generated as the output of a linear system where the input is the recorded traces (Spitz, 1991). The benefit of this method is that it does not require prior knowledge of the coherency of the traces.

Additionally, the data was band-passed with a filter 0.001 MHz/0.01 MHz/0.8 MHz/1.2 MHz window, the same filter used in the bone plate experiments. The data was debiased by zero-averaging the traces. The traces were self-normalized for plotting.

2.3 Data Analysis

Frequency Spectra

Using MATLAB, frequency spectra were obtained for the *in vitro* and *in vivo* data sets by transforming the traces to the frequency domain with a one-dimensional fast Fourier transform. In order to better view the frequency content of the data, the individual traces were smoothed. Smoothing was achieved by convolving the trace with a Hamming window. The length of the Hamming window chosen was 1/40 the length of the trace.

Spectral Decomposition

Spectral decomposition, or time-frequency ($t - f$) analysis, is an inversion method that decomposes a signal such that the frequency distribution can be viewed in time for an individual trace. This tool provides useful information about the variation of spectral energy in time.

In the $t - f$ domain, spectral decomposition is able to separate modes of different frequency arriving coincident in time (Prosser, Seale and Smith, 1999). The experimental data has non-stationary signals and a frequency distribution that varies with time, so $t - f$ analysis is an ideal tool.

The method we used was developed by Bonar and Sacchi (2010) and involves a multi-wavelet approach. This approach deconvolves the ultrasound signal with a series of different frequency wavelets. This method works as follows: an incident ultrasound signal reflects on an interface with an impedance contrast. The reflected wavelet is treated as a convolution of the incident signal with the reflectivity of the interface. The reflectivity function can, in turn, be obtained by deconvolving the source wavelet and the reflected signal. In a multi-wavelet decomposition, each ultrasound trace is considered a convolution of the reflectivity function with a dictionary of Ricker wavelets of various frequencies. A Ricker wavelet is defined by its centre frequency (Ryan, 1994). Complex Ricker wavelets were used to obtain phase information. A Ricker wavelet dictionary is deconvolved from the ultrasound to return a frequency-dependent reflectivity function; this can be transformed to generate the $t - f$ map (Bonar and Sacchi, 2010).

To improve the resolution of the result, a joint l_1 and l_2 norm strategy was used. The decomposition was posed as an inverse problem to minimize a cost function with an l_2 norm prediction error term and an l_1 norm regularization term. The l_1 regularization term increases the solution resolution and results in a sparser solution than an l_2 regularization term. An l_2 norm was used to fit the data.

Phase Velocity versus Frequency Map

In order to study the dispersive characteristics of the data, we mapped the data to the frequency-phase velocity ($f - c$) domain. The $f - c$ domain is of particular interest as the dispersion of guided wave modes is apparent in the $f - c$ space. A two-dimensional Fourier transform was applied to the $x - t$ ultrasound traces to map the data to the frequency-wavenumber ($f - k$) space (Alleyne and Cawley, 1991). Aliasing in the frequency domain was avoided using a low-pass filter to remove the wavenumber and frequency components larger than the Nyquist. The $f - k$ data was mapped to the frequency-phase velocity domain using the relation $c = 2\pi f/k$. To better visualize guided wave modes, the loci of the maximum intensity energy clusters in the $f - c$ map were picked using an automatic picking program. This program picked the maximum energy points on the $f - c$ map above a specified threshold. The threshold was set as 0.30 of the maximum energy; points on the $f - c$ map with energy above the threshold were picked for different regions of the map so that each guided wave mode could be isolated.

Singular Value Decomposition

In order to reduce noise in the *in vivo* human tibia data set, a singular value decomposition (SVD) was implemented. The SVD was used to isolate the desired body wave and guided wave components from the residual signal, which includes the high frequency noise.

The use of SVD as a signal processing technique was first developed in geophysics and is based on linear algebra matrix diagonalization. The SVD is able to isolate wave components in the data. This method can isolate the high-velocity, early-arriving or the late-arriving guided wave region by removing incoherent energy from the signal.

The SVD of an $m \times n$ matrix A is given by

$$A = UDV^T. \tag{4}$$

where U is composed of the eigenvectors of AA^T , D is a diagonal $m \times m$ matrix of singular values, and V is composed of the eigenvectors of $A^T A$ (Zhao and Chen, 2011). The singular values are ordered from largest to smallest, and the largest amplitude singular values contribute most to the construction of matrix A . A cut-off value, ε , is chosen based on the energy distribution associated with the singular values. The matrix A is reconstructed with equation (4) using a new D matrix where the singular values smaller than the cut-off value are set to be zero. This retains only the singular values larger than the cut off value.

Before the SVD was performed, the data was reprocessed to time-shift the chosen wave packet so that it appears as a flat event. This was done to improve trace correlation and coherency and this shift allows for the chosen wave packet to be separated from the rest of the signal. After the SVD, the time shift was reversed to return the data to its initial form.

First, as SVD was performed to isolate the guided wave region of the data. Next, an SVD was performed to isolate the body wave portion of

the data. These two results were added together to generate the final SVD image. This two-pronged SVD approach enabled the SVD to remove noise from both wave packets in the data.

2.4 Waveform Simulation

We performed a numerical simulation to generate synthetic ultrasound traces for the *in vitro* bone plate model. To generate the simulated response, we used the reflectivity method used in seismology (Kind, 1976; Kennett, 1983). This method assumes an isotropic and laterally homogenous layered model consisting of a set number of layers overlying a half-space.

The reflectivity method was first proposed by Thompson (1950). This method was later modified to study surface wave dispersion in multi-layered media (Haskell, 1953). This technique calculates the surface response of the stratified media over a half-space using a propagator matrix algorithm (Gilbert and Backus, 1966), which propagates the wavefield through the material layers. The ultrasound source is implemented as a strike-slip discontinuity at the surface of the model. The tension axis of the discontinuity is aligned with the incident angle of the ultrasound source in the transducer-wedge system (24.4°). The receiving direction is also oriented with that of the ultrasound receiving transducer-wedge system.

The result of the numerical simulation represents the full wavefield response for a set of boundary and initial conditions. The solution is

represented as a double improper integral over radial frequency (ω) and horizontal wavenumber (k). As the wave-number (calculated by $k = \omega/c$) is dependent on phase velocity (c), the k integration is limited by the phase velocity range. The ω -integral is performed by an inverse FFT to the time domain, and the solution is band-limited. The reflectivity method accurately takes into account all possible reflections, transmissions, internal multiples and mode conversions.

The computer codes used to generate the reflectivity synthetics were developed by professor Jeff Gu of the Department of Physics, University of Alberta. A similar stratified approximation has been previously used to successfully model ultrasound body waves in long bone (Le et al., 2010). Two models were used to simulate the wavefield through the BP and STBP models, respectively. Synthetic traces were simulated for a model based on bone parameters used in a previous study ($v_{\text{compressional}} = 4000$ m/s, $v_{\text{shear}} = 1970$ m/s, $\rho = 1.93$ kg/m³, with absorption coefficients $\alpha_{\text{compressional}} = 5$ dB/MHz/cm and $\alpha_{\text{shear}} = 11$ dB/MHz/cm) (Le et al., 2010). The homogenous layered model consisted of a 9 mm thick bone layer overlying a water half-space. The water half-space below acted as a marrow mimic. For the soft tissue experiment, a 2.5 mm layer was added to the model; this layer had the same material properties as the Aqualene couplant used in the experiment.

2.5 Theoretical Dispersion Modeling

To interpret the frequency-phase velocity maps of the *in vitro* data, theoretical dispersion curves were generated for the low-frequency guided wave modes. The dispersion curves were calculated and plotted with the commercial program DISPERSE, version 2.0.16B (Imperial College, London). A plate model consisting of isotropic, homogenous layers was used, which was the same model used in the numerical waveform simulation. The generated theoretical dispersion curves are determined by numerically solving the dispersion relation. An example of the dispersion relationship for a bone plate bounded above and below by air is given by equation (1). The generated dispersion curves are a function of frequency and phase velocity so can be superimposed on the $f - c$ maps of the experimental data. The fundamental (A_0, S_0) and first order (A_1, S_1) Lamb modes were generated.

Chapter 3

Results

3.1 Bone Plate

The ultrasound data exhibits two distinctive wave packets of different velocities: the early-arriving, high-frequency body waves and the late-arriving, low-frequency guided waves (Fig 3.1). The early-arriving wave packet represents a direct wave and is attenuated at far offset. The slower wave packet is high-amplitude at far offset and exhibits a dispersive wave train.

Figure 3.2 displays 20 out of 130 traces of the same data set. Superimposed on the image are the predicted travel times of three wave arrivals: a direct compressional wave, a shear wave, and a Rayleigh wave. The velocities used to model these arrivals ($v_{\text{compressional}} = 4000$ m/s, $v_{\text{shear}} = 1970$ m/s, and $v_{\text{Rayleigh}} = 1840$ m/s) are characteristic of ultrasound velocity in bone and have been successfully used in other studies (Le et al., 2010). To account for the transit time in the transducer wedges, the predicted travel times were translated by $5 \mu\text{s}$; this value was calculated from the distance travelled in the wedge and the material velocity. The predicted compressional wave arrival is consistent with the FAS. This arrival is non-dispersive and low-amplitude at far offset, as expected for a body wave arrival. The shear wave arrival is slower and is not a distinct arrival in the

experimental data as shear waves are considerably lower amplitude than compressional waves. The Rayleigh wave arrival closely follows the shear wave arrival and corresponds to the high amplitude guided wave. As plate thickness increases, the velocity of a Lamb wave approaches that of a Rayleigh wave (Nicholson et al., 2002). Given the ease of calculating the Rayleigh velocity, a Rayleigh wave was used to predict the guided wave arrival time. This velocity is calculated by the cubic equation (Le et al., 2010) using $v_{\text{compressional}} = 4000 \text{ m/s}$ and $v_{\text{shear}} = 1970 \text{ m/s}$.

The one-dimensional Fourier transform of the data displays the frequency maxima of individual traces. The spectrum was smoothed with a 101-point Hamming window. The spectra of the BP data set are shown for two offsets, 40 mm and 140 mm (Fig. 3.3). At close offset, where the body wave region is prominent, there is a range of frequency content. The maximum frequency peak is at 0.54 MHz. There is a low-frequency maximum (0.22 MHz) as well as two higher frequency local maxima (0.70 MHz and 0.84 MHz). At far offset (Fig 3.3b), the BP trace only shows a strong low-frequency peak at 0.12 MHz.

The time-frequency plots allow us to see the evolution of the frequency content of the data through time (Fig. 3.4). The $t - f$ panels for the BP model are displayed at three offsets: 40 mm, 90 mm, and 140 mm. The ultrasound trace at 120 mm offset is displayed beside the corresponding $t - f$ map. At close offset, there is a strong, high-frequency signal early in time (Fig 3.4a), and this signal decays in the mid- and far-offset cases (Fig 3.4b, c). In the 90 mm and 140 mm cases, a strong low-frequency guided wave energy cluster is visible at 0.12 MHz. At 140 mm,

the low-frequency guided wave energy is bound between 90 and 130 μs ; it lines up with the guided wave arrival in the time signal (Fig. 3.4d).

The results of the numerical simulation have lower frequencies than the bone plate data, but still show the two characteristic wave arrivals (Fig. 3.5). The simulation exhibits an early-arriving body wave section and a slow, low-frequency guided wave section. The same predicted arrival times used in the *in vitro* image (see Fig. 3.6) are superimposed on the numerical data.

To compare the synthetic to the experimental data, we examined the guided wave section of an individual trace at 140 mm. This distance was chosen as the guided waves are dominant at that offset and the early-arriving body waves do not interfere with the late-arriving guided waves. To isolate the guided wave, the simulated trace was generated for a limited range of phase velocities, (800 m/s to 2500 m/s) which cuts out the faster-travelling body waves. The synthetic trace was band-pass filtered up to 0.30 MHz. The experimental data was windowed to isolate the guided waves and the same band-pass filter used on the synthetics was applied to the experimental data. Figure 3.7 shows that the numerically simulated data plotted against the experimental data. The comparison agrees well at low frequency and the phases of the arrivals are consistent. The correlation between the two traces is high, with a correlation coefficient of 0.8726.

The dispersive characteristics of the guided waves were studied with an $f - c$ map. Two main energy clusters are observed (Fig. 3.8). The theoretical dispersion curves are superimposed to aid in the identification

of guided wave modes. There is a low-frequency, low-velocity cluster at approximately 0.12 MHz and 1500 m/s that has very high amplitude. This represents most of the $f - c$ energy and corresponds to the A_0 guided wave mode. There is another mode around 2100 m/s and 0.22 MHz; it is considerably less prominent and corresponds to the S_0 mode. The loci of the maximum energy in the $f - c$ map were picked and displayed in Fig. 3.9. The two strong energy clusters detected in the experimental data are the fundamental Lamb modes, A_0 and S_0 (Fig. 3.9), while only the A_0 mode is detected in the simulated data (Fig. 3.9).

3.2 Soft Tissue Bone Plate

The $x - t$ image for the STBP data shows two distinct wave packets (Fig. 3.10). The high-frequency, early-arriving body wave packet is still intact and there is considerable ringing in the signal. In the presence of soft tissue, the late-arriving, guided wave packet has a high-frequency component; the guided waves are not visibly lower frequency than the body wave arrival. The guided wave region has a shortened wave train.

The STBP traces are plotted with the lateral compressional wave arrival, lateral shear wave arrival and Rayleigh wave arrival (Fig 3.11). In the soft tissue experiment, the FAS is not a direct wave, but a lateral compressional wave that travels through the soft tissue and along the bone plate (Camus et al., 2000). In order to account for the transit time in both the soft tissue and the wedge, these arrivals were translated in time by 7 μ s. The calculated travel time in the wedge is 5 μ s and the remaining 2 μ s

accounts for the additional transit time through the soft tissue. The velocities of the predicted arrivals are the same as used for the BP data set. The plotted lateral P-wave is consistent with the FAS. The lateral shear wave arrival is not detectable in the data. The Rayleigh wave arrives shortly after the shear wave arrival and corresponds to the guided wave arrival.

The frequency spectra for the STBP are displayed for two offsets, 40 mm and 140 mm, which represent the close and far offset cases. At close offset (Fig. 3.12a), there are two strong maxima (0.22 MHz and 0.45 MHz), as well as a series of high-frequency peaks of lower amplitude. At far offset (Fig 3.12b), where the guided waves are prominent, there are three maxima (0.10 MHz, 0.36 MHz and 0.81 MHz). The plot is smoothed with a 101-point Hamming window.

In the STBP case, the $t - f$ exhibits a high-frequency, high-energy signal present at all offsets (Fig 3.13). This signal maintain a high amplitude at far offset, and is visible as the late arriving guided wave packet in the time signal from 90 to 110 μs (Fig 3.13d). The low-frequency guided wave signal is present at 0.1 MHz (Fig 3.13c) and is much lower amplitude in comparison to the high-frequency signal. This signal is weak and the high-frequency signal dominates the $t - f$ map.

Two wave packets are seen in the numerical simulation: a weak early-arriving body wave and a high-frequency, late-arriving guided wave (Fig 3.14). Though the synthetic results are low-frequency, they still exhibit the two characteristic wave arrivals. The predicted arrivals are superimposed on 20 synthetic traces (Fig. 3.15). The body wave arrival is

weak, but still apparent. The shear wave arrival is not discernable in the data, as expected. The Rayleigh wave corresponds to the low-velocity, high-frequency dispersive wavetrains visible in the data.

The STBP experimental and synthetic traces at 140 mm offset were compared in the same manner as for the BP data. The comparison demonstrates that the experimental data agrees well with the simulated data at low frequency and the phases are consistent (Fig 3.16). The correlation between the two traces is low with a coefficient of 0.5436. While the two traces correlate well in phases but the amplitudes are different in magnitude.

The guided wave region of the STBP data was further examined with an $f - c$ map. There are two strong clusters of energy present in the $f - c$ map (Fig. 3. 17). There is a cluster of low-frequency, low-velocity energy at approximately 0.05 MHz to 0.2MHz between 1300 m/s and 2500 m/s. This includes energy from modes A_0 , S_0 and A_1 . The second group of energy includes A_1 and S_1 (approximately 0.35 MHz and 1700 m/s). Additionally, there is some high-velocity energy from 0.2 – 0.4 MHz; this signal is not as strong amplitude as the lower velocity energy clusters and falls into the range of body wave velocities. This energy did not correspond with any of the theoretical dispersion curves. In general, the $f - c$ energy is spread out fairly evenly between the low-frequency modes.

The maximum intensity loci of the $f - c$ map were picked, and plotted along with the generated theoretical dispersion curves (Fig. 3.18). In the experimental data, four guided wave modes are present: A_0 , S_0 , A_1 and S_1 . The simulated data expresses only the A_0 and S_0 modes.

3.3 *In Vivo* Human Tibia

The human tibia data was interpolated to reduce the spacing interval from 2 mm to 1 mm; this matches the sampling interval of the *in vitro* data. The interpolated human tibia data shows the two previously studied wave groups (Fig 3.19): the fast arriving body waves are visible as well as the slow-arriving guided waves. The guided wave exhibits a dispersive wave train, but the guided wave arrival is complicated by the fact that some reverberated body wave signal is still present in the guided wave region. The body wave arrival includes multiple reflections and reverberations; this signal is attenuated at far offset. Though the data has a low signal-to-noise ratio, the two characteristic arrivals are still distinct and identifiable.

The predicted wave arrivals were applied to the data (Fig. 3.20) using the same values used for the bone plate images. To line up the predicted arrivals with the wave arrivals in the tibia data, the travel times were shifted 11 μs in time. The calculated transit time of ultrasound in the wedge is 5 μs and the remaining 6 μs is accounted for by the soft tissue. The compressional wave arrival lines up with the FAS in the HT data. The lateral shear wave arrival is too weak to discern on the image. The Rayleigh wave arrival matches the guided wave arrival.

The frequency spectra for the human tibia data are shown for two offsets, 40 mm (Fig 3.21 a) and 140 mm (Fig 3.21 b). The spectrum was smoothed with an 87-point Hamming window. The close offset trace has

three frequency maxima (0.32 MHz, 0.47 MHz and 0.75 MHz), with the centre peak being the most prominent. The far offset trace has one strong maximum at 0.16 MHz. There is a small series of higher frequency peaks in the far offset data, including smaller maxima at 0.71 MHz and 0.95 MHz.

The $t - f$ plots are given for three offsets: 40 mm (Fig 3.22a), 90 mm (Fig. 3.22b) and 140 mm (Fig 3.22c). In the 40 mm trace, the signal is dominated by a band of high-frequency energy (0.4 MHz – 0.8 MHz) that is present throughout the entire time signal. At 90 mm, some lower frequency energy is visible in the data, but it is dominated by the high-frequency signal. The low-frequency energy was centred on 0.2 MHz. At far offset (140 mm), the guided wave portion is higher energy and lower frequency (0.12 MHz from 100 μ s – 130 μ s). The time signal (Fig 3.22d), exhibits considerable noise, which generates some of the high-frequency signal in the $t - f$ space. The highest amplitude portion of the trace is in the guided wave region where the strongest $t - f$ signal is.

The $f - c$ map displays two strong clusters of energy (Fig. 3.23). There is some low-frequency, low-velocity energy (0.10 MHz – 0.25 MHz and 1700 m/s). The majority of the $f - c$ energy is high-velocity (3200 m/s to 5000 m/s). There is additional high-velocity high-frequency energy visible, but it is low-amplitude.

The *in vivo* data has a low signal-to-noise ratio, so an SVD was implemented to separate wave components in the data and remove noise. The SVD was performed in two steps. First the guided wave region of the data was isolated with an SVD, and then the same procedure was followed

to isolate the body wave section. To isolate the body wave, the cut off was set as 6 and this retained 38% of the energy of the original data. For the guided wave, the cut-off was set as 7, and this retained 24% of the original energy. These two results were added together to generate the final SVD image. The combined SVD result represents 62% of the energy of the original HT data. In both steps, the high frequency noise was separated from the desired wave component as a residual signal. The resultant data (Fig 3.24) shows the two wave arrivals very distinctly; the high-frequency noise is greatly removed.

The frequency content for the SVD data shows more distinct frequency peaks and a drop off of the high frequencies (Fig 3.25). The close offset (Fig 3.25a) image has one strong maximum (0.46 MHz), while the far offset (Fig. 3.25b) has one strong maximum (0.17 MHz).

The $t - f$ map for the SVD is greatly altered. The high-frequency signals visible in the original are greatly diminished and the low-frequency signal is very prominent (Fig 2.26). A high-frequency signal is visible in the $t - f$ plot, but it is low amplitude at far offset. The low-frequency guided wave signal is visible at mid- and far-offset (Fig 2.26b, c) and represents the highest energy signal in the $t - f$ space. The high-frequency signal at 140 mm offset (Fig 2.26c) matches up with the high amplitude part of the trace (Fig 2.26d).

To generate the $f - c$ map for the SVD filtered data, the guided waves were isolated in the SVD then windowing was used to remove artifacts from the body waves. There are two main regions of spectral energy visible in the $f - c$ plot (Fig. 2.27). There is a high-velocity cluster

visible, and a lower energy cluster that represents the low-frequency low-velocity guided wave.

A second human tibia, denoted HT2, set was obtained. The same parameters and processing procedures were applied to this data set. The guided wave and body wave arrivals are present in this data. Figure 3.28 shows the HT2 data set alongside the primary HT data set (Fig 3.28).

The frequency content of the second human tibia experiment is shown alongside that of the HT data set at offsets of 40 mm (Fig 3.29a, c [HT, HT2 resp.]) and 140 mm (Fig 3.29b, d [HT, HT2 resp.]). At close offset, the HT2 data has four high frequency maxima (0.32 MHz, 0.52 MHz, 0.74 MHz, and 0.87 MHz). At far offset, there is a strong maximum at 0.11 MHz as well as two lower-amplitude, higher frequency maxima (0.48 MHz, 0.60 MHz).

The $f - c$ map for the secondary HT2 data set was also examined (Fig. 3.30 b) alongside the HT data (Fig 3.30a). The majority of the $f - c$ energy is high-velocity (2500 m/s - 5000 m/s). There is also a low-frequency, low-velocity cluster of energy (0.1 MHz - 0.2 MHz at 1500 m/s to 2000 m/s).

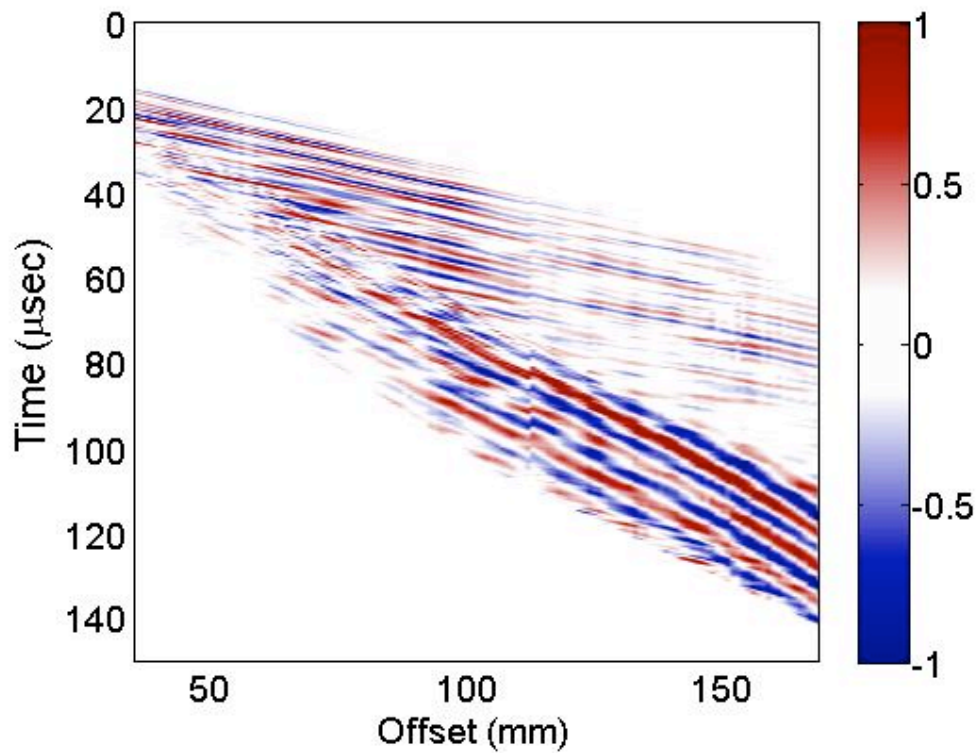


Figure 3.1 The $x - t$ diagram of the ultrasound signals for the BP. The records are self-normalized. The positive and negative values represent the normalized amplitudes of the individual traces.

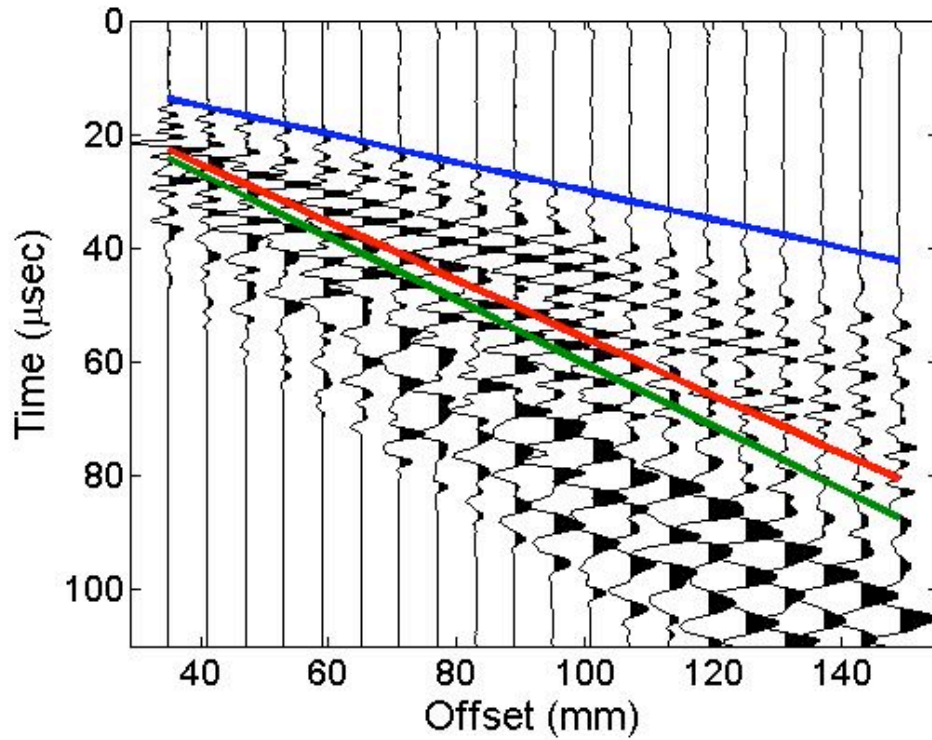


Figure 3.2 The $x - t$ diagram of the ultrasound time signals for the BP. The image displays 20 out of 130 columns of the matrix in “wiggly” format. The records are self-normalized. Superimposed are the arrival times of the compressional wave (blue), shear wave (red), and Raleigh wave (green). The velocities of these arrivals are as follows: $v_{\text{compressional}} = 4000$ m/s, $v_{\text{shear}} = 1970$ m/s, and $v_{\text{Rayleigh}} = 1840$ m/s.

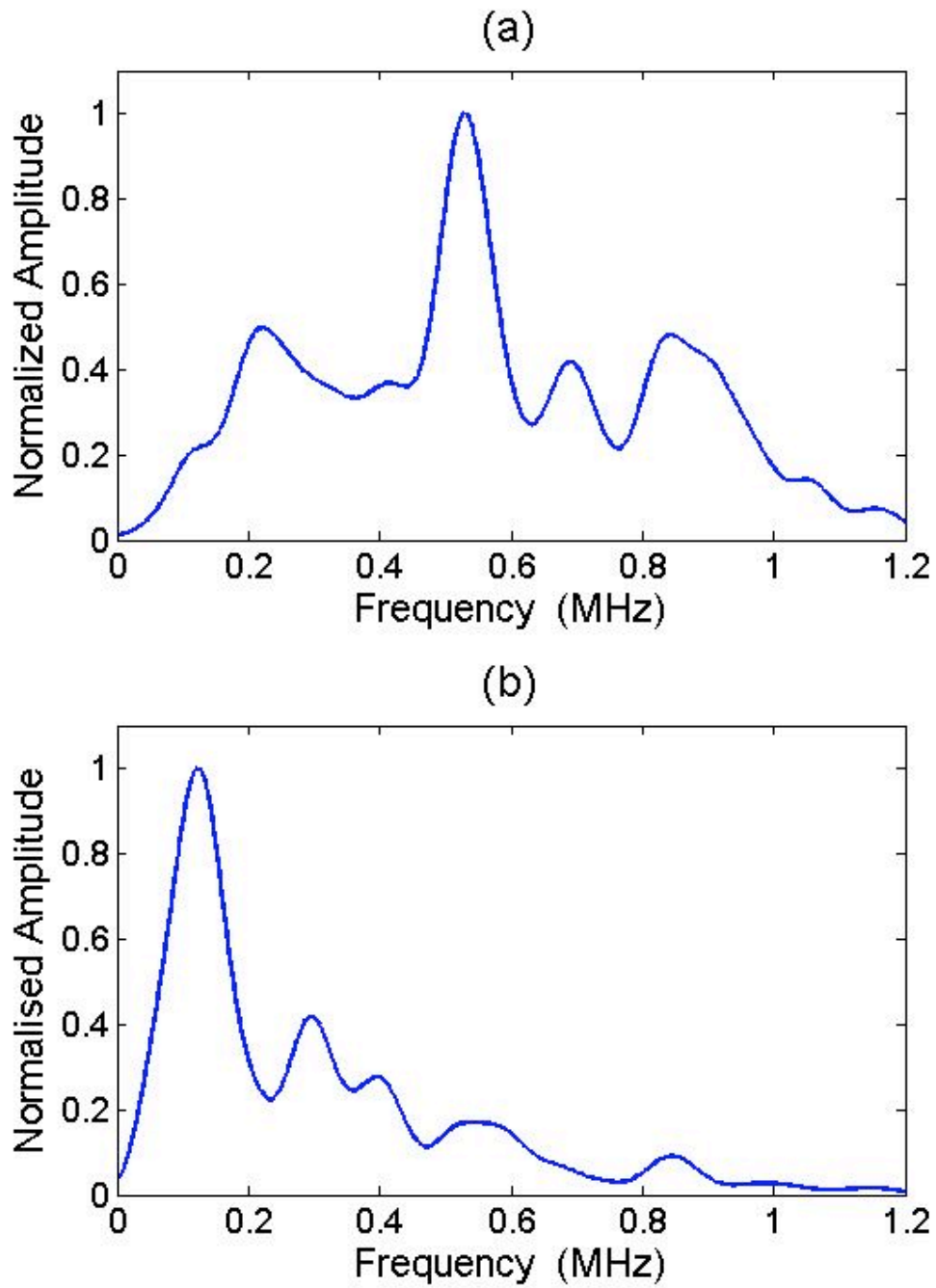


Figure 3.3 The BP amplitude spectra at two offsets: (a) 40 mm and (b) 140 mm. The spectra are self-normalized.

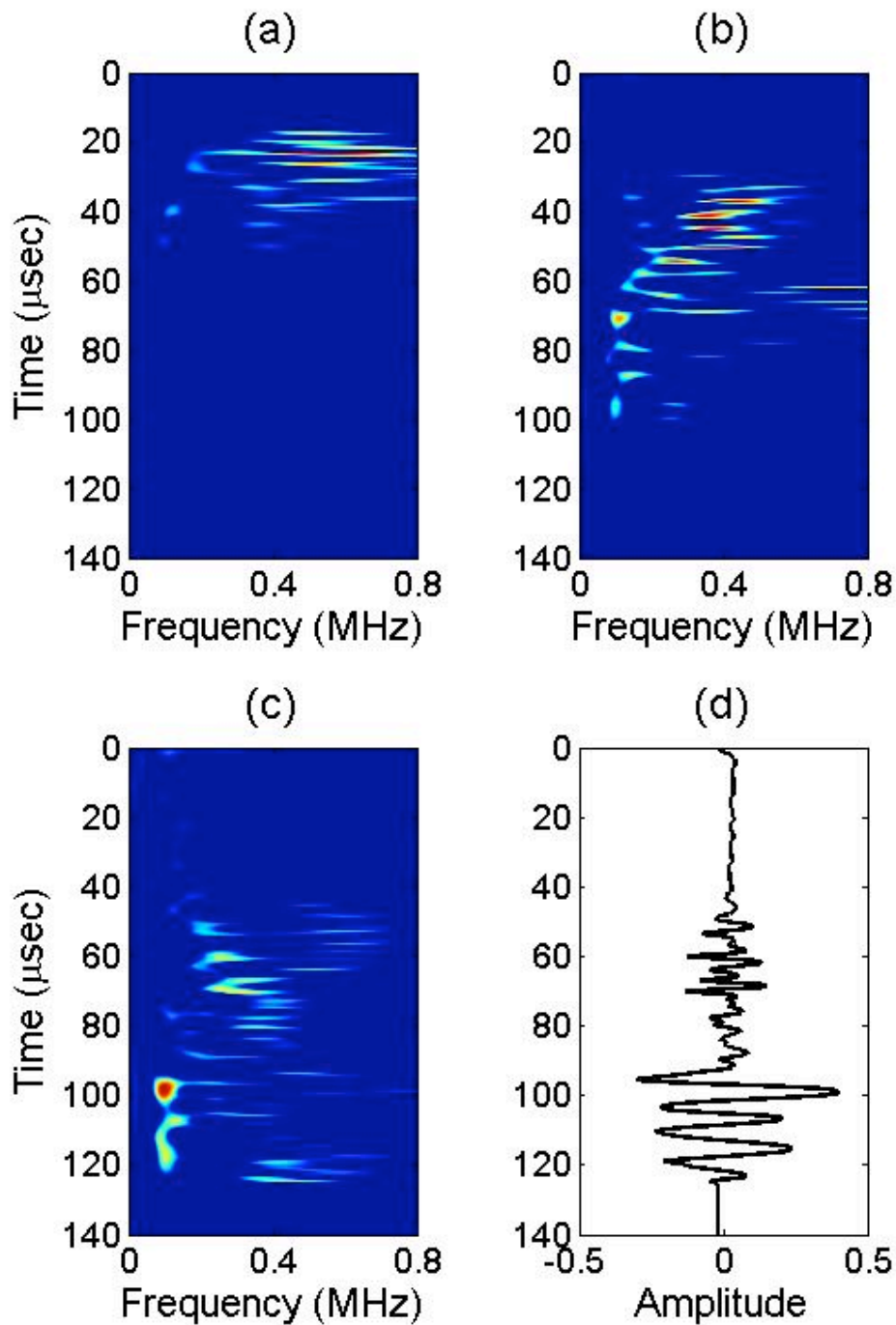


Figure 3.4 The $t - f$ plots for the BP at offsets 40 mm (a), 90 mm (b), and 140 mm (c). Also plotted is the time signal for (d) the bone plate at 140 mm offset.

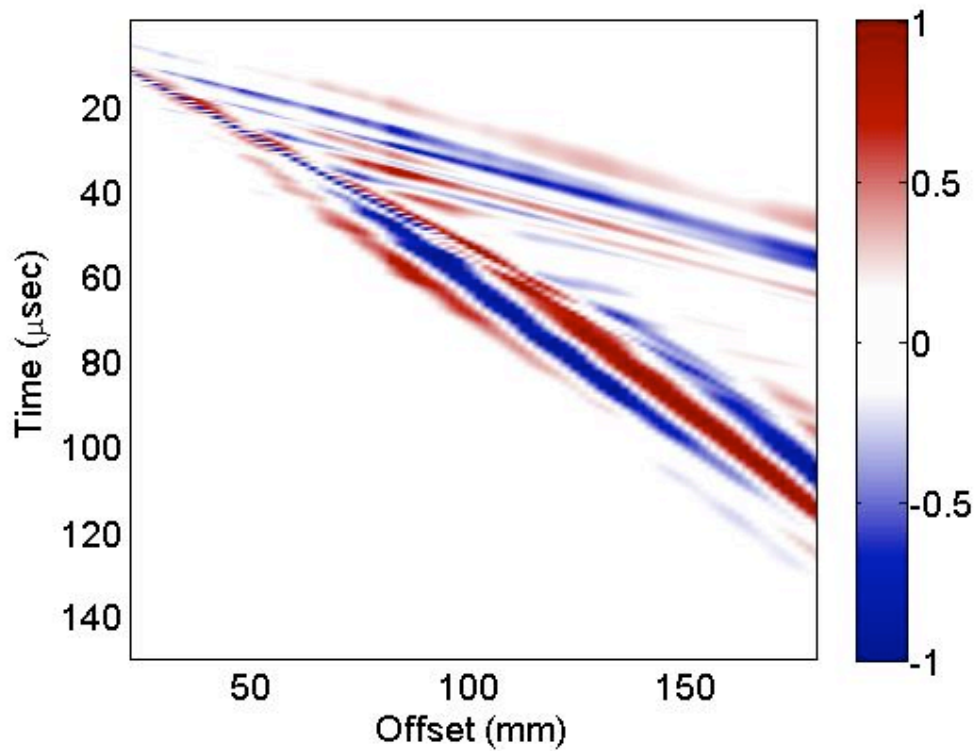


Figure 3.5 The $x - t$ diagram of the numerically simulated BP traces. The records are self-normalized.

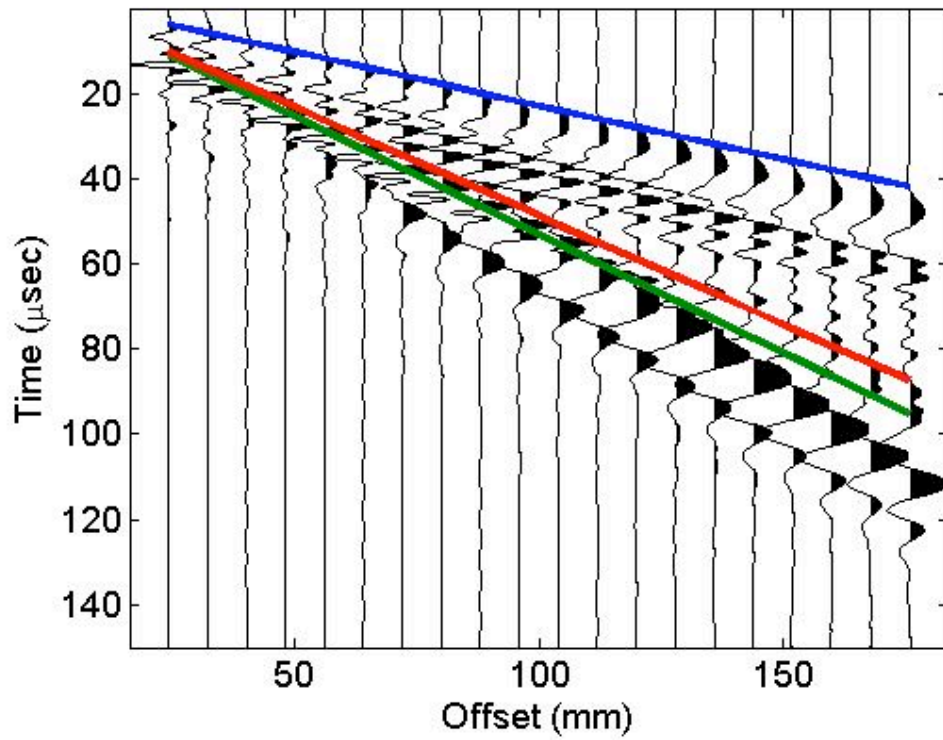


Figure 3.6 The $x - t$ diagram of the numerically simulated BP traces. The records are self-normalized. Superimposed are the arrival times of the compressional wave (blue), shear wave (red), and Rayleigh wave (green).

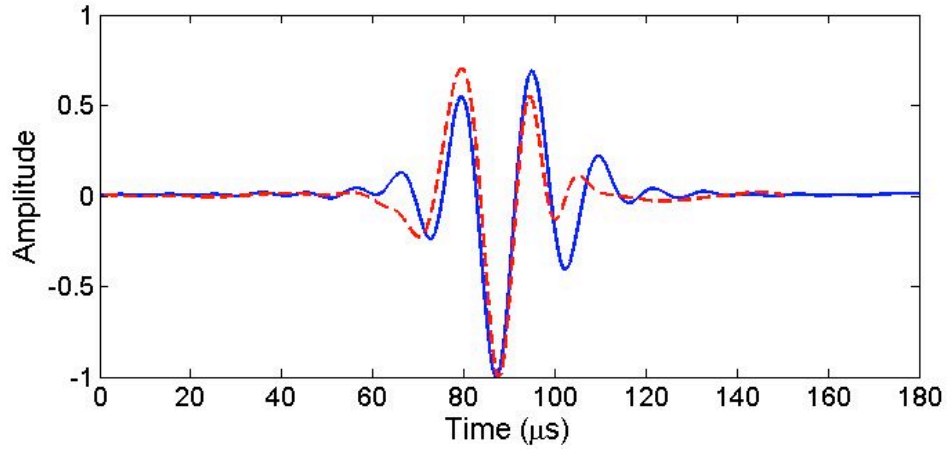


Figure 3.7 Comparison of experimental (blue solid curve) and numerically simulated (red dashed curve) signals at 140 mm offset for the BP.

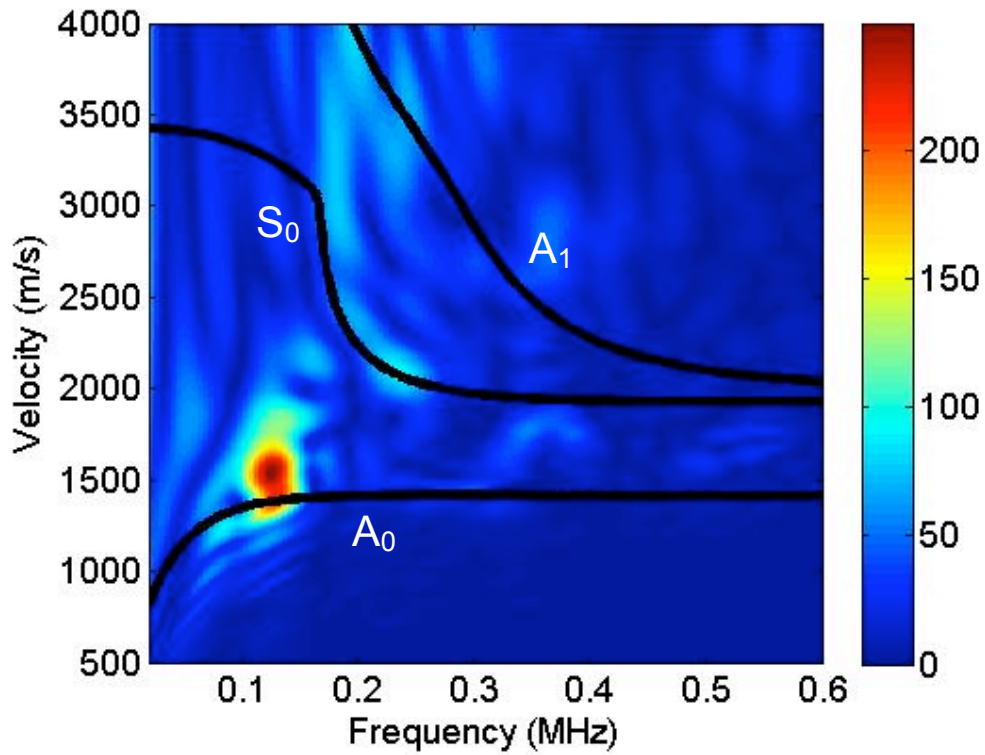


Figure 3.8 The $f - c$ diagram for the BP data with theoretical dispersion curves (black solid lines) superimposed.

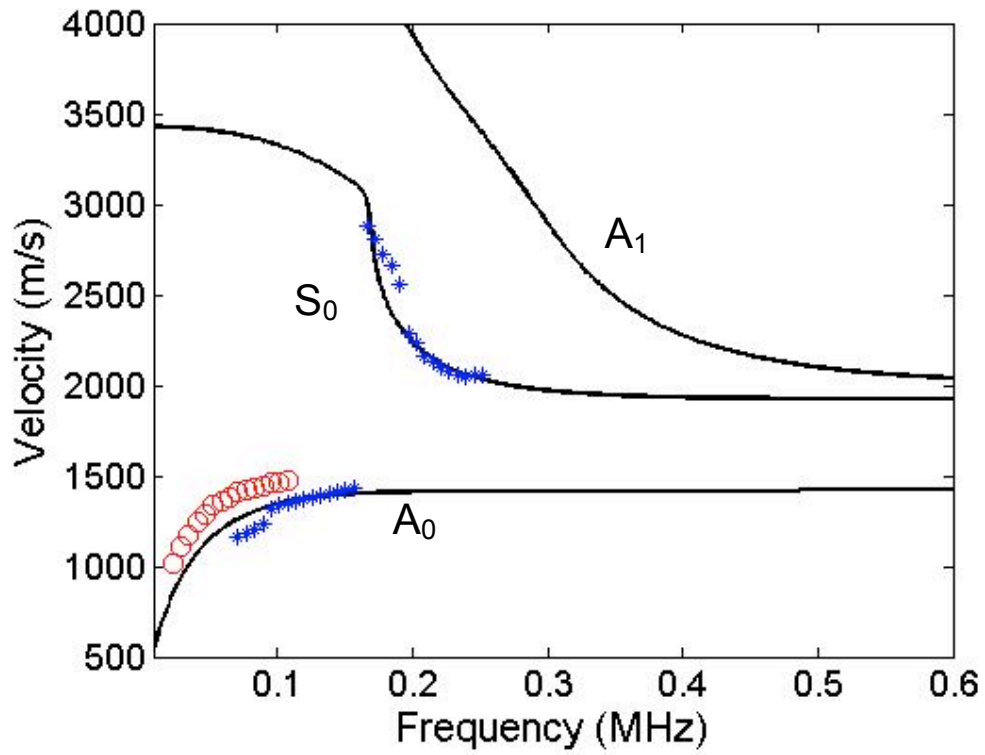


Figure 3.9 Theoretical $f - c$ dispersion curves (black solid curves) for the BP data. Superimposed are the picked maximum intensity points from the experimental data (blue stars) and simulated data (red circles).

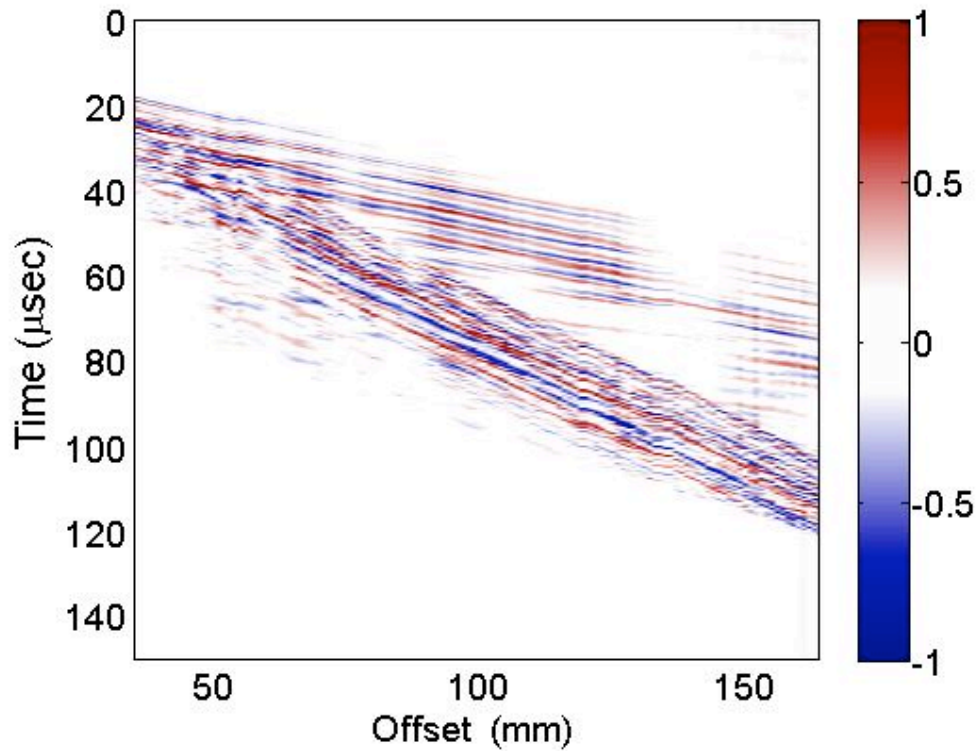


Figure 3.10 The $x - t$ diagram of the ultrasound signals for the STBP. The records are self-normalized.

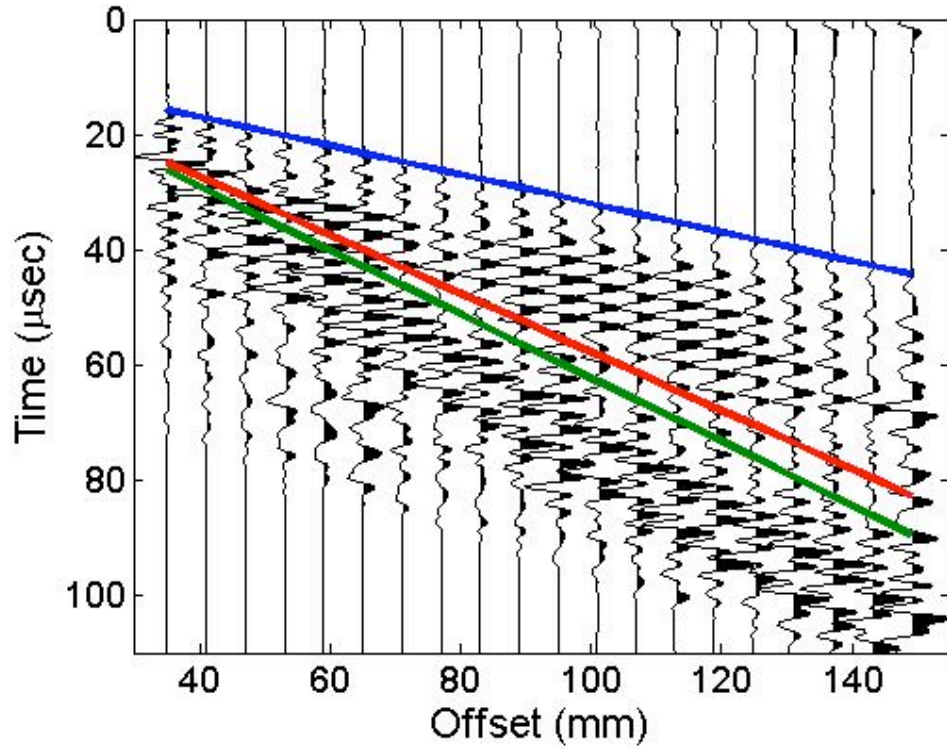


Figure 3.11 The $x - t$ diagram of the ultrasound STBP traces. The records are self-normalized. Superimposed are the arrival times of the compressional head wave (blue), shear wave (red), and Raleigh wave (green); (The velocities of these arrivals are as follows: $v_{\text{compressional}} = 4000 \text{ m/s}$, $v_{\text{shear}} = 1970 \text{ m/s}$, and $v_{\text{Rayleigh}} = 1840 \text{ m/s}$).

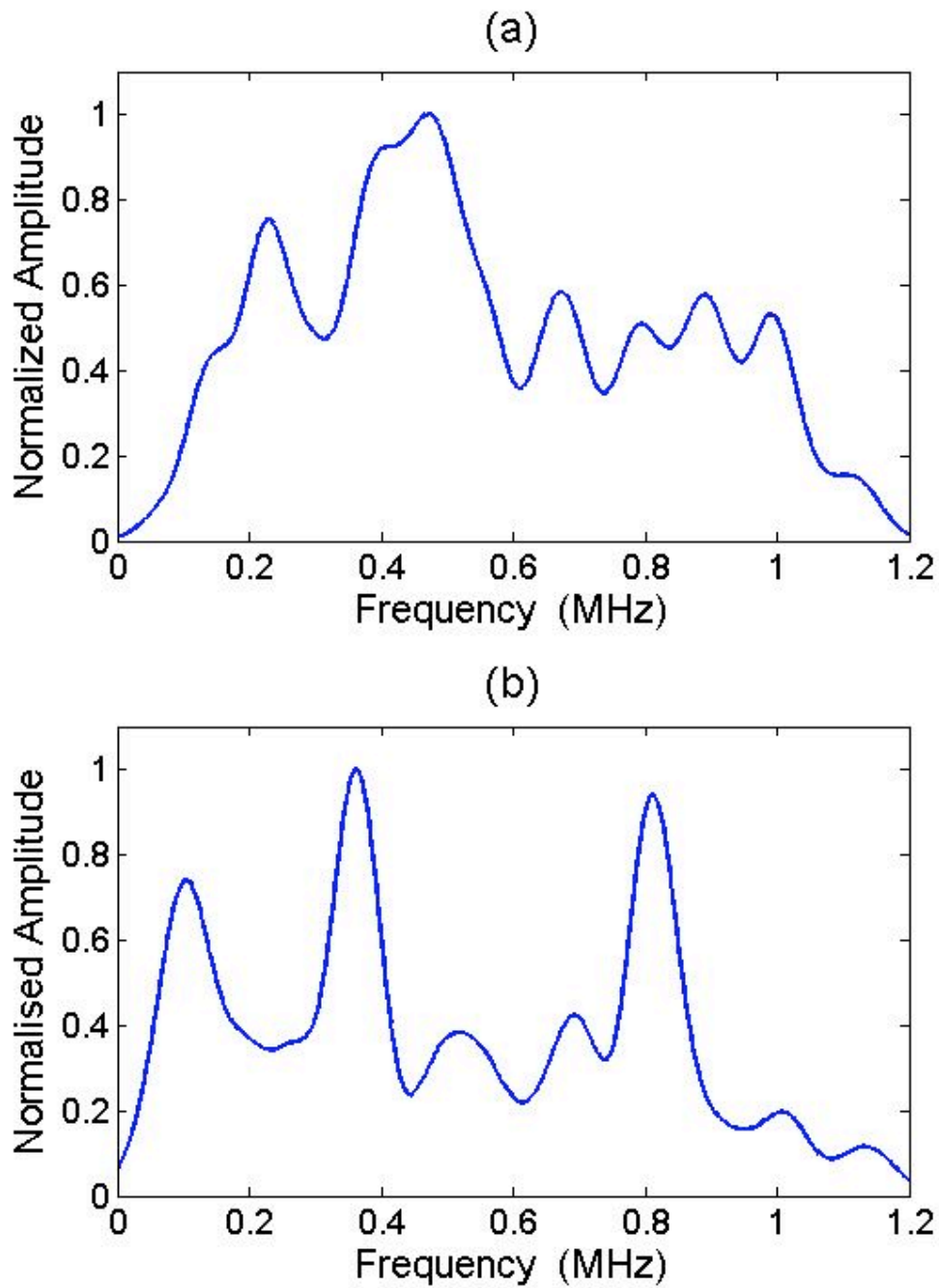


Figure 3.12 The amplitude spectra for the STBP data at two offsets: (a) 40 mm and (b) 140 mm. The spectra are self-normalized.

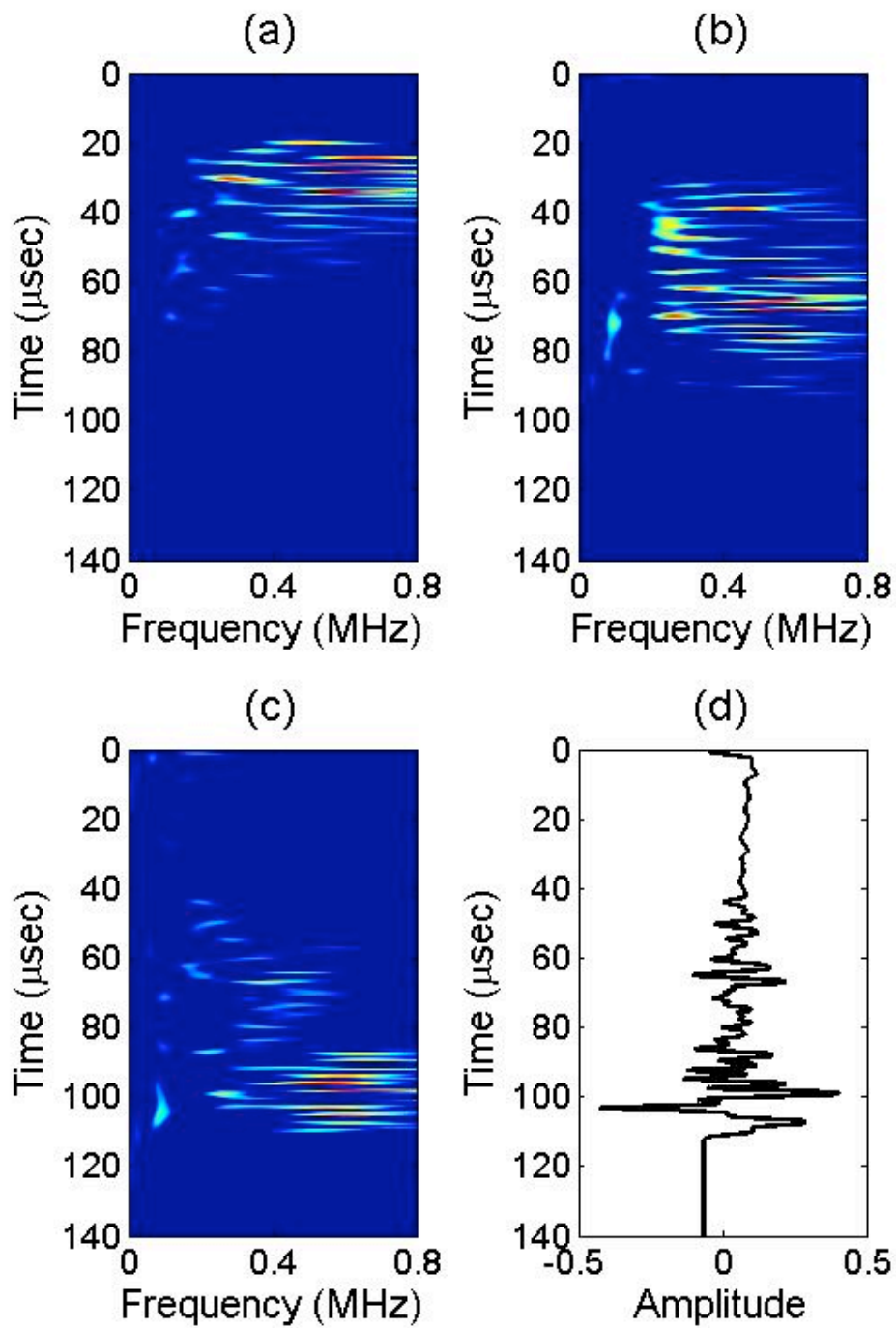


Figure 3.13 The $t - f$ plots for the STBP data at offsets 40 mm (a), 90 mm (b), and 140 mm (c). Also plotted is the time signal for (d) the STBP at 140 mm offset.

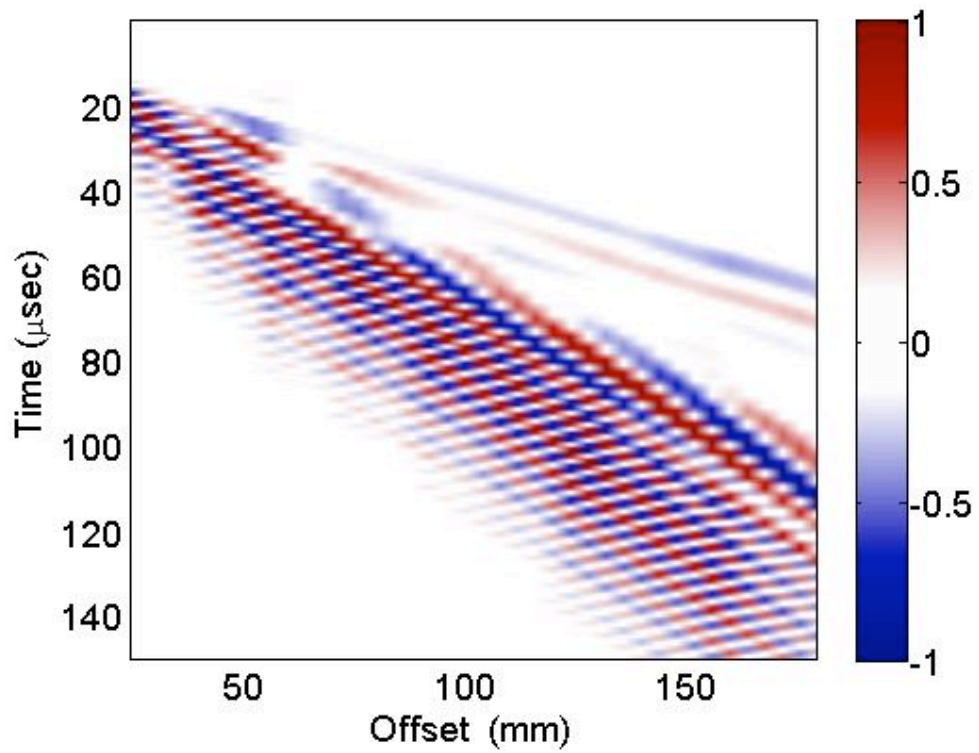


Figure 3.14 The $x - t$ diagram of the numerically simulated STBP traces. The records are self-normalized.

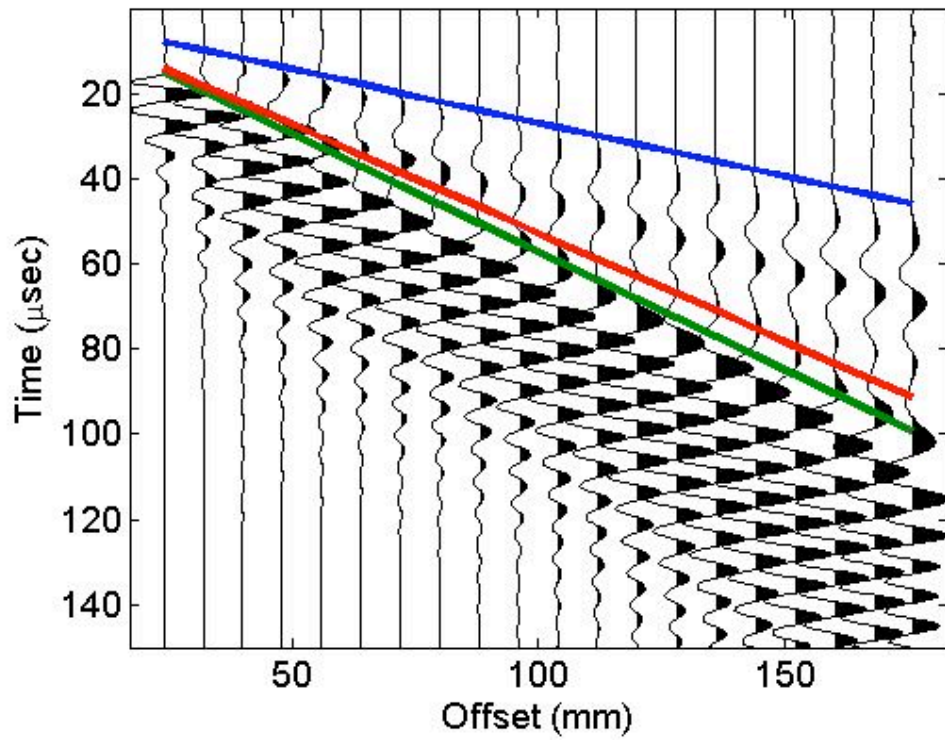


Figure 3.15 The $x - t$ diagram of the numerically simulated STBP traces. The records are self-normalized. Superimposed are the arrival times of the compressional wave (blue), shear wave (red), and Rayleigh wave (green).

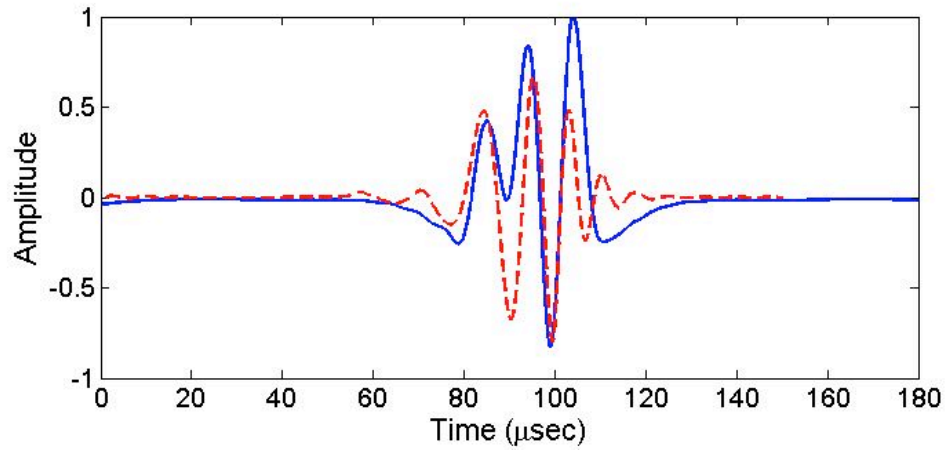


Figure 3.16 Comparison of experimental (blue solid curve) and numerically simulated (red dashed curve) traces at 140 mm offset for the STBP data.

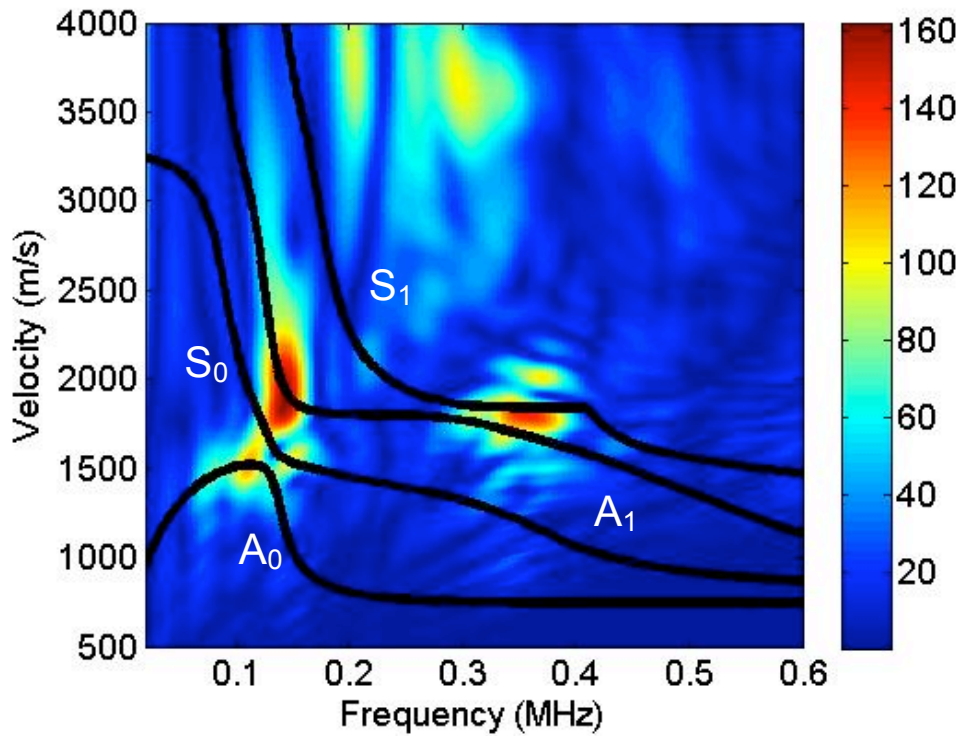


Figure 3.17 The $f - c$ diagram with theoretical dispersion curves (black solid lines) superimposed.

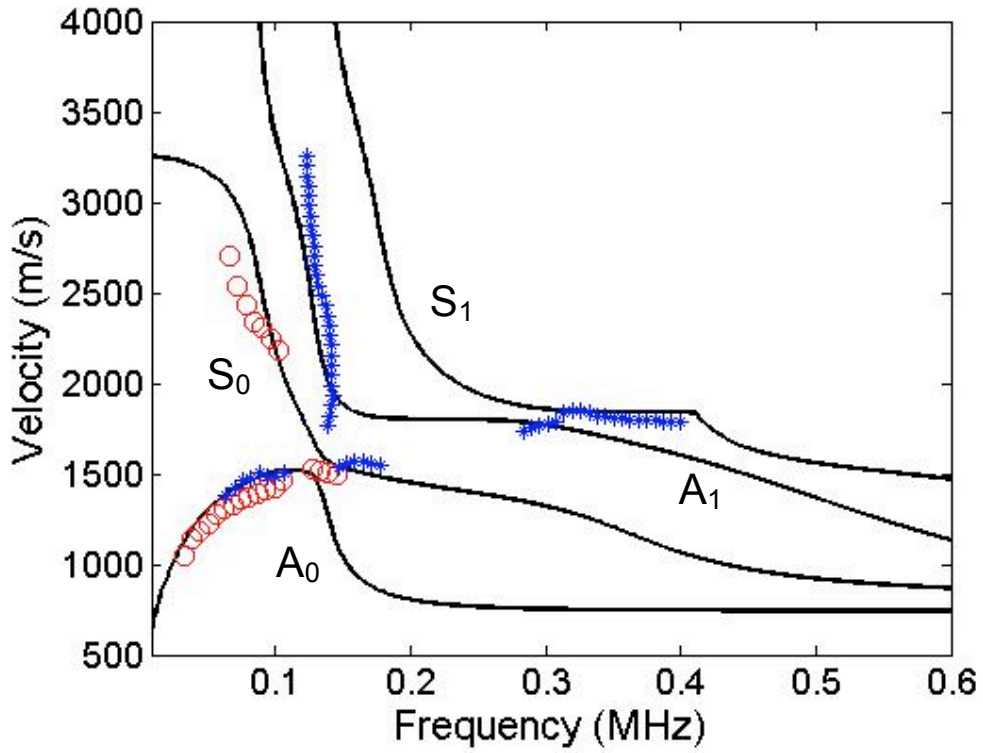


Figure 3.18 Theoretical $f - c$ dispersion curves (black solid curves) for the STBP data. Superimposed are the picked maximum intensity points from the experimental data (blue stars) and simulated data (red circles).

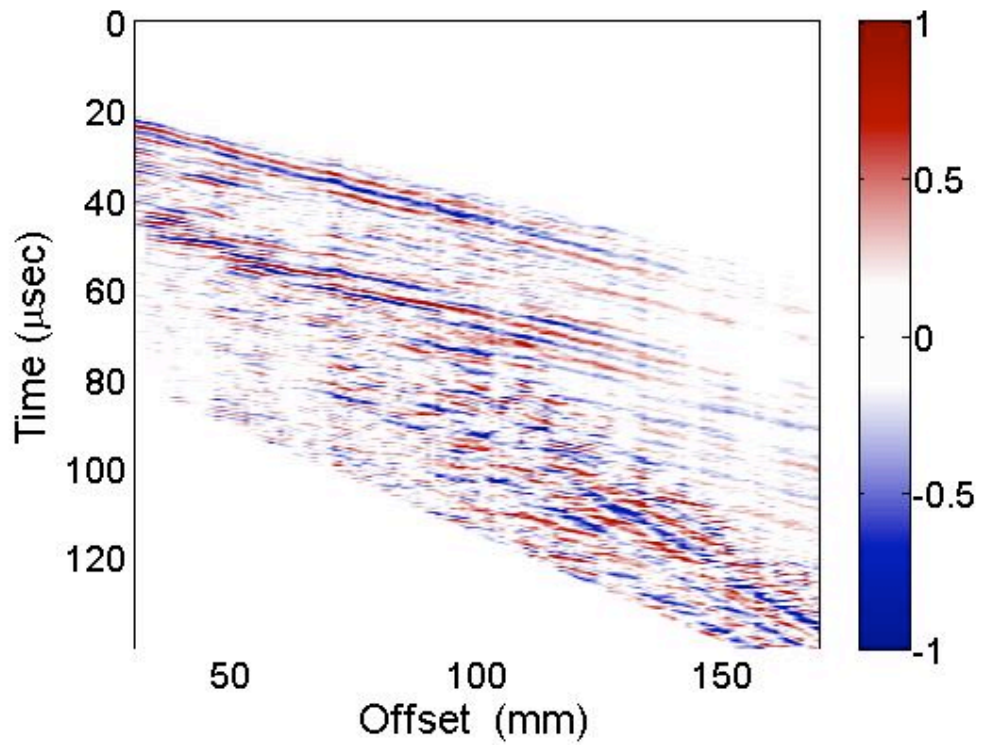


Figure 3.19 The $x - t$ diagram of the ultrasound signals for the HT traces. The records are self-normalized.

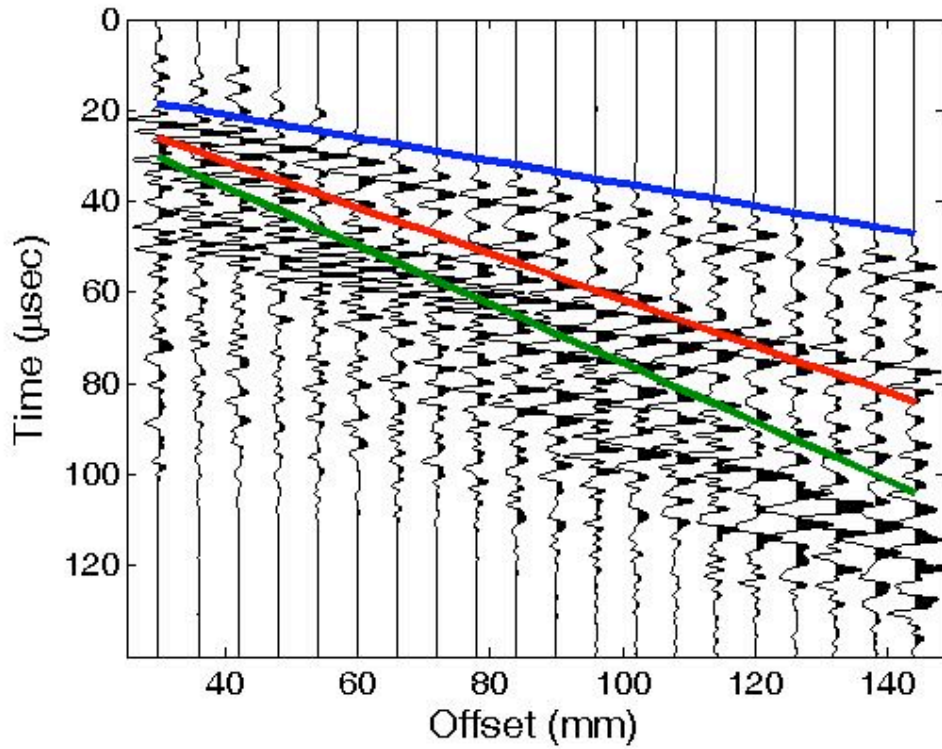


Figure 3.20 The $x - t$ diagram of the ultrasound traces for the HT data. The records are self-normalized. Superimposed are the arrival times of the compressional head wave (blue), shear wave (red), and Raleigh wave (green).

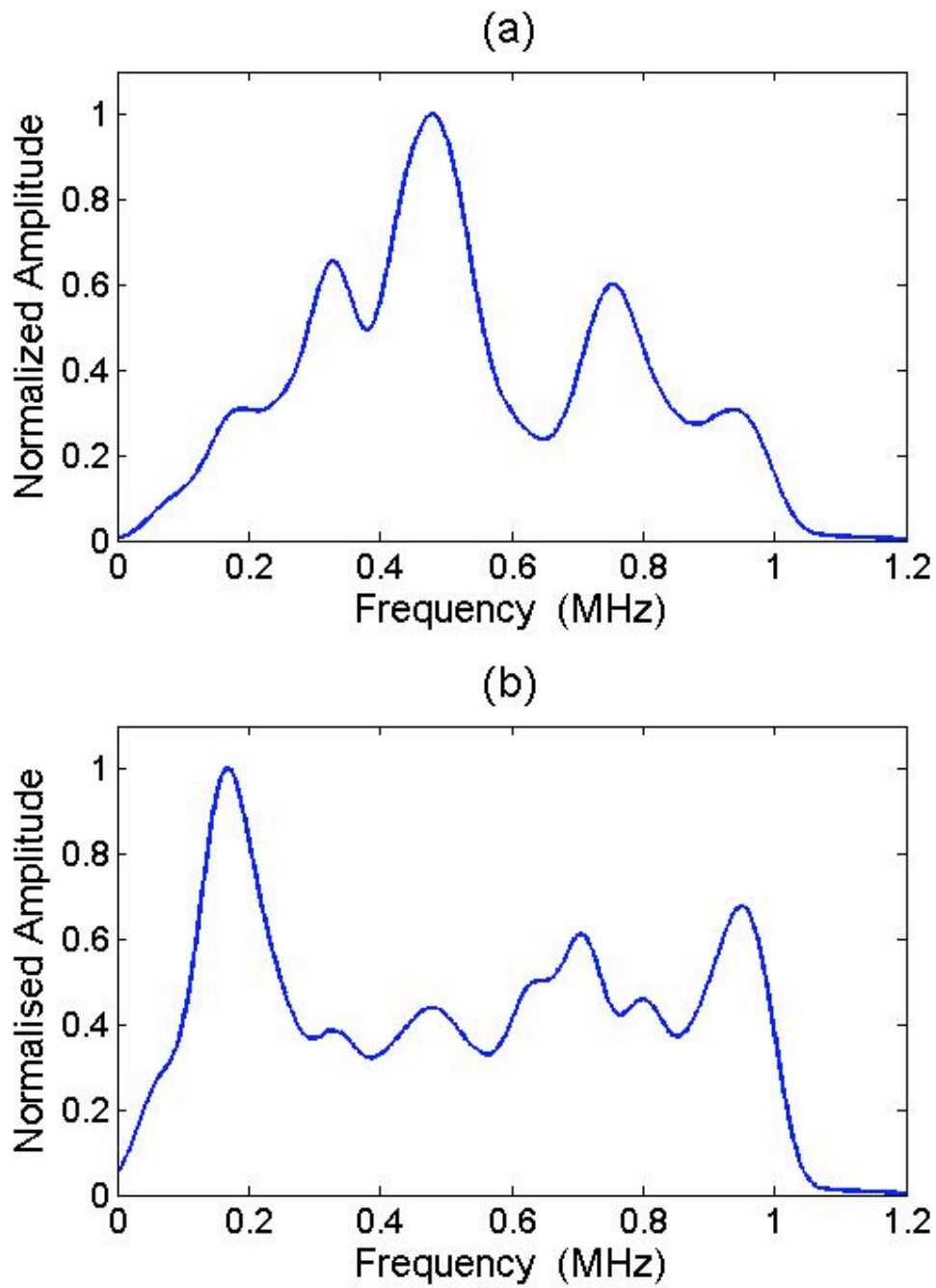


Figure 3.21 The HT amplitude spectra at two offsets: (a) 40 mm and (b) 140 mm. The spectra are self-normalized.

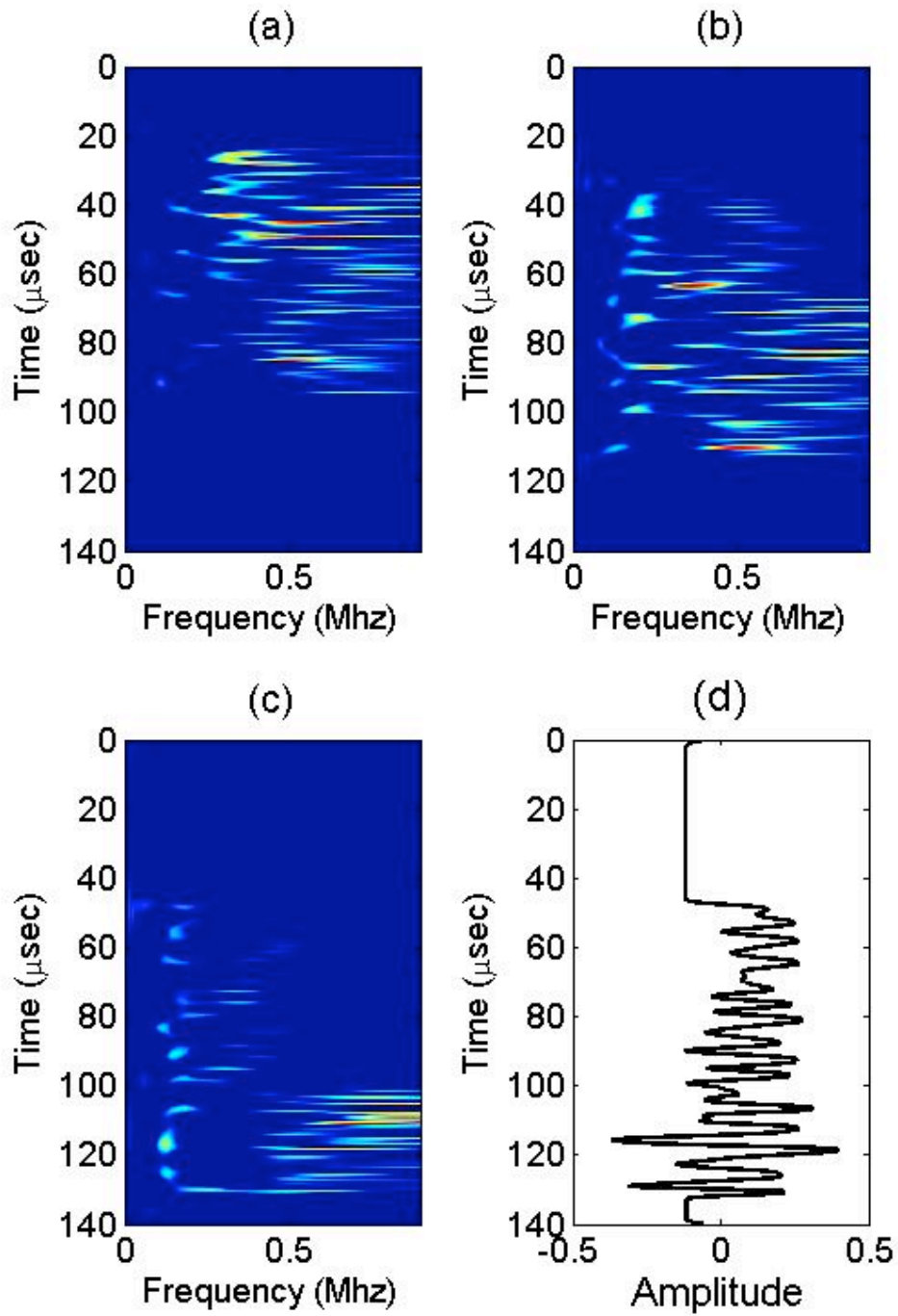


Figure 3.22 The $t - f$ plots for the HT at offsets 40 mm (a), 90 mm (b), and 140 mm (c). Also plotted is the time signal for (d) the HT data at 140 mm offset.

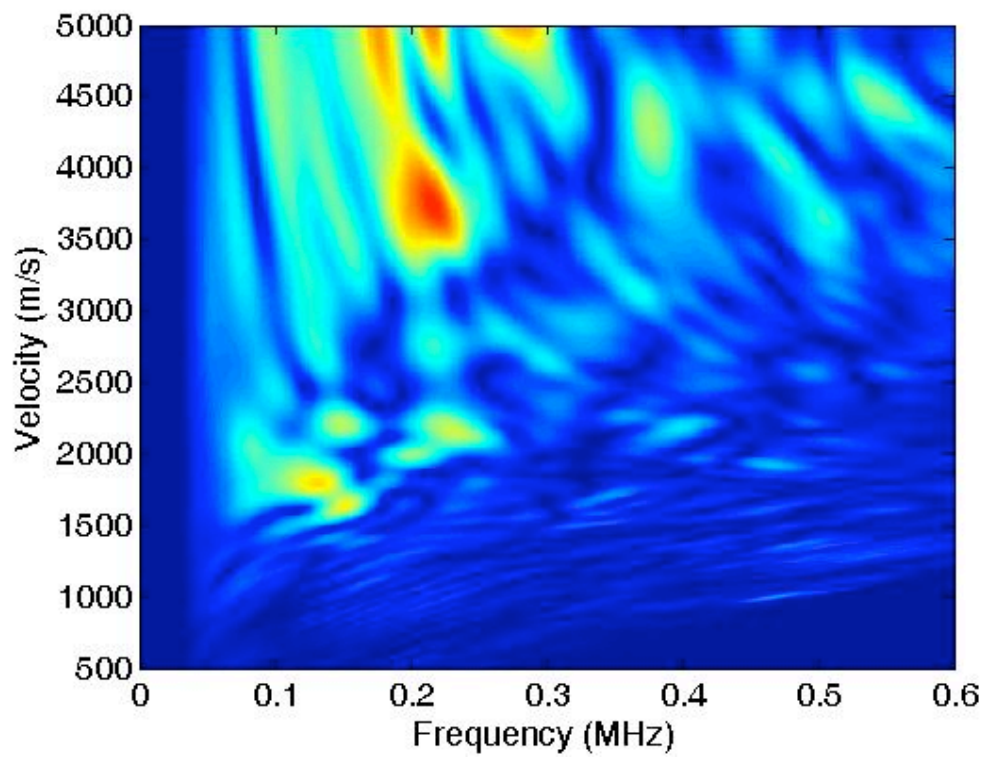


Figure 3.23 The $f - c$ diagram for the HT data.

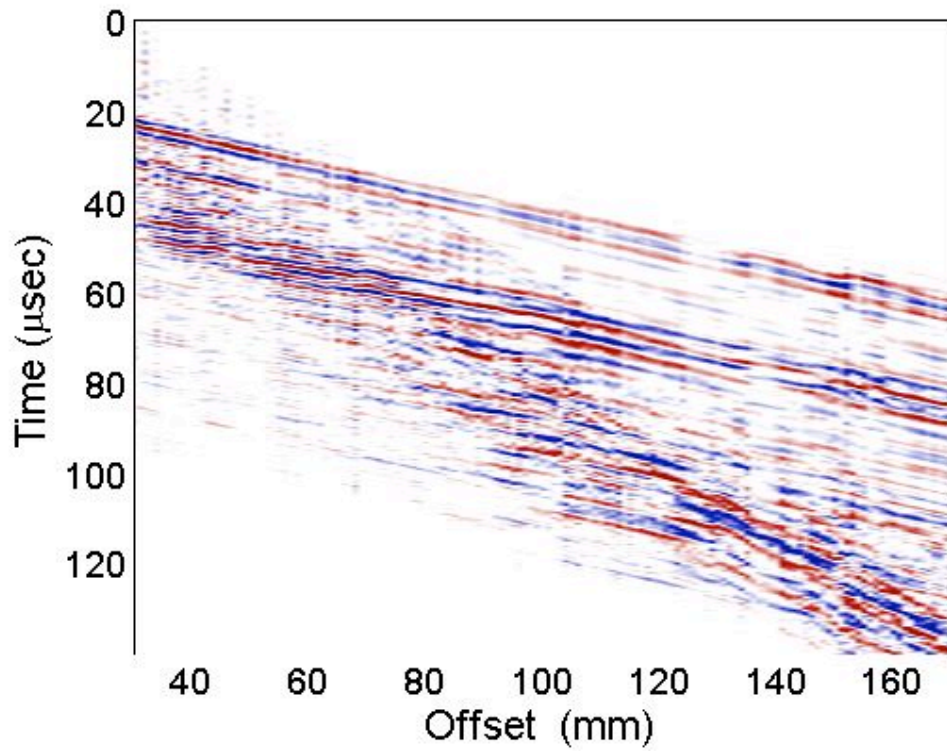


Figure 3.24 The $x - t$ diagram of the ultrasound signals for the HT SVD results. The records are self-normalized.

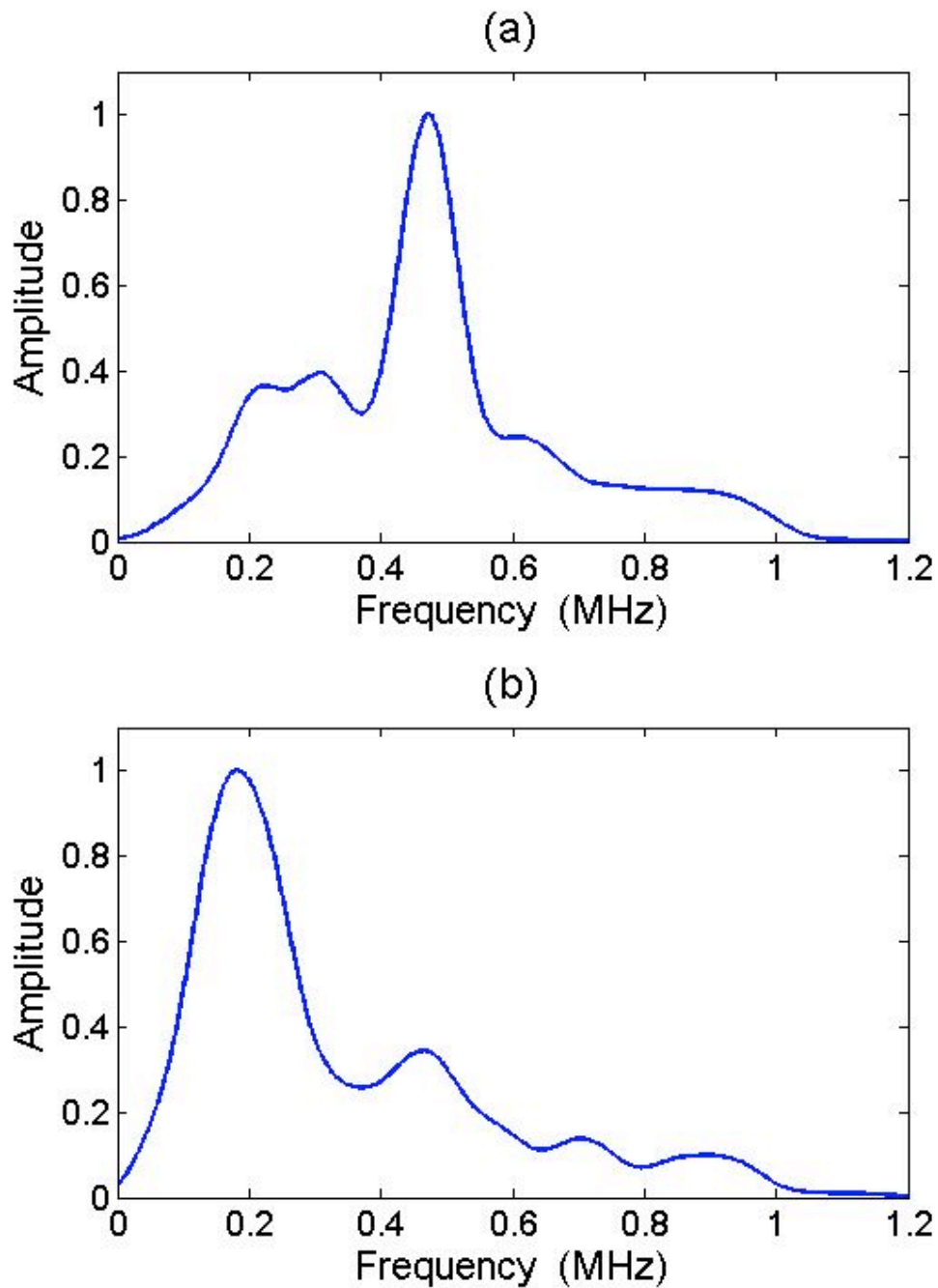


Figure 3.25 The amplitude spectra of the SVD HT data at two offsets: (a) 40 mm and (b) 140 mm. The spectra are self-normalized.

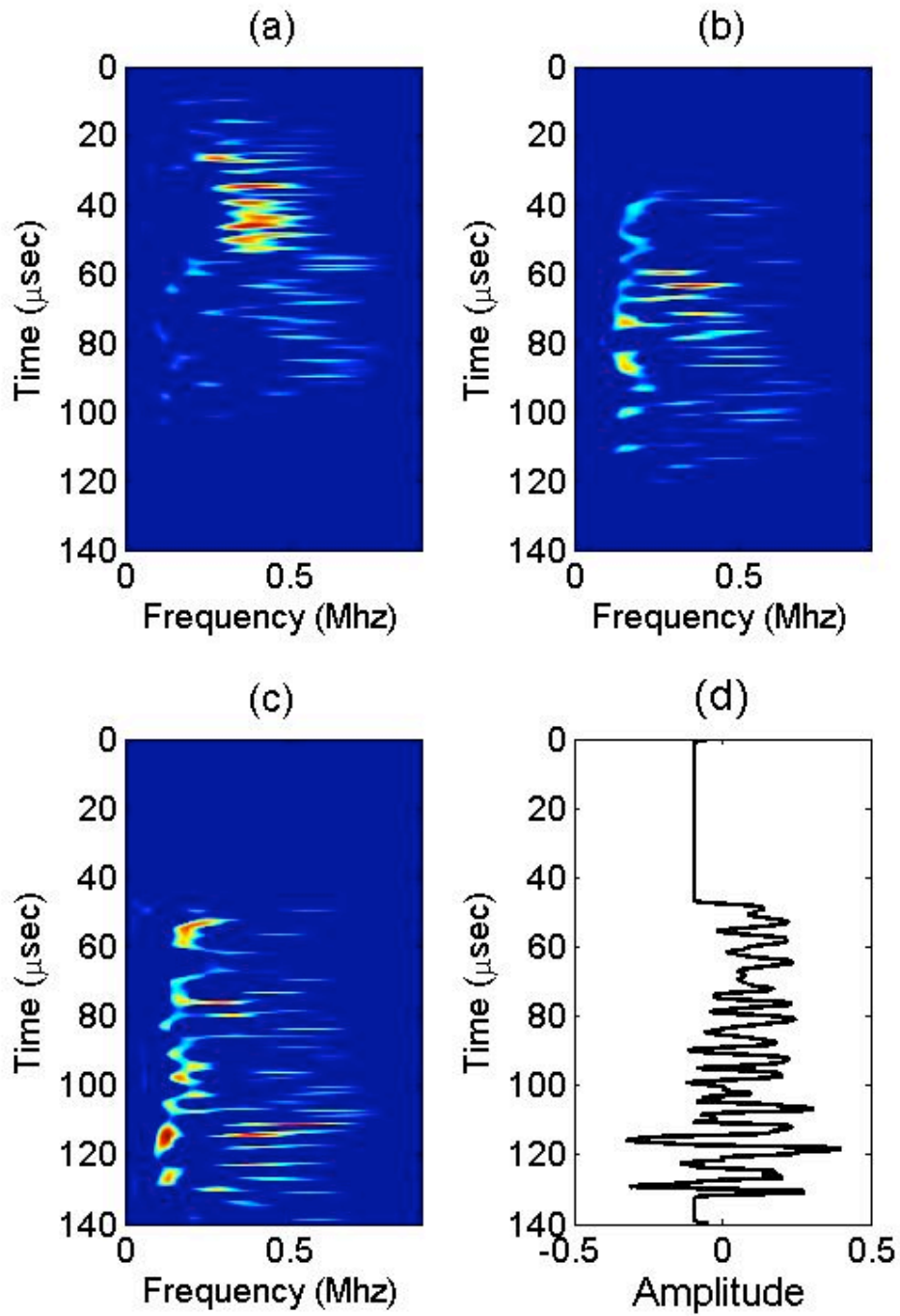


Figure 3.26 The $t - f$ plots for the HT SVD data at offsets 40 mm (a), 90 mm (b), and 140 mm (c). Also plotted is the time signal for (d) the data at 140 mm offset.

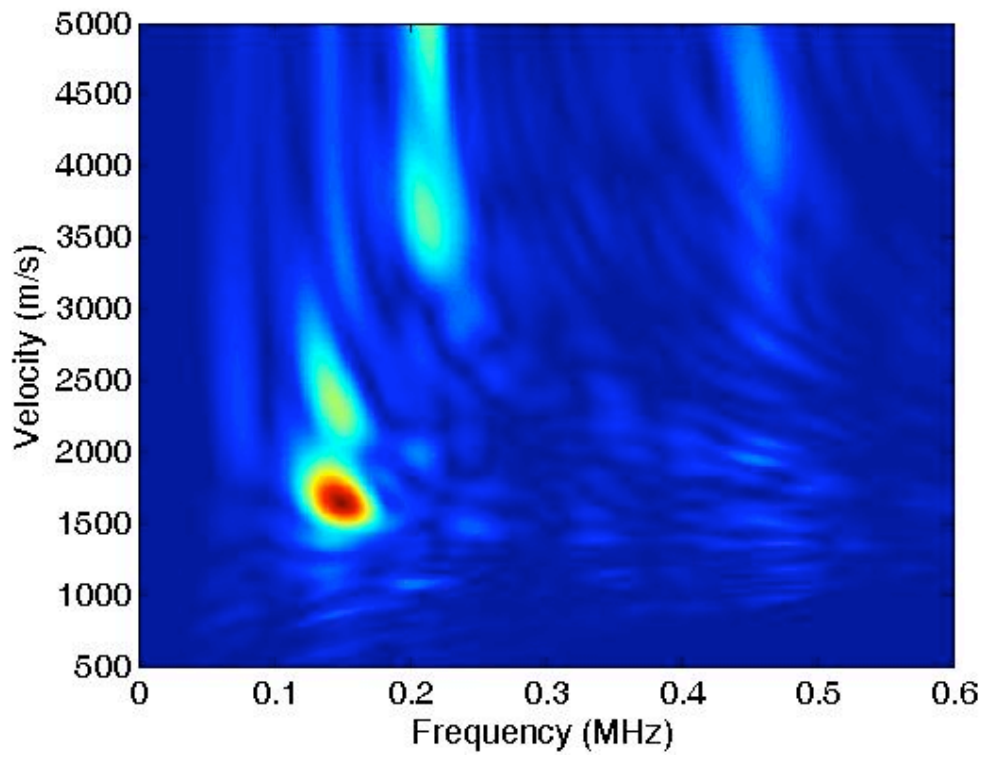


Figure 3.27 The $f-c$ diagram for the HT SVD results.

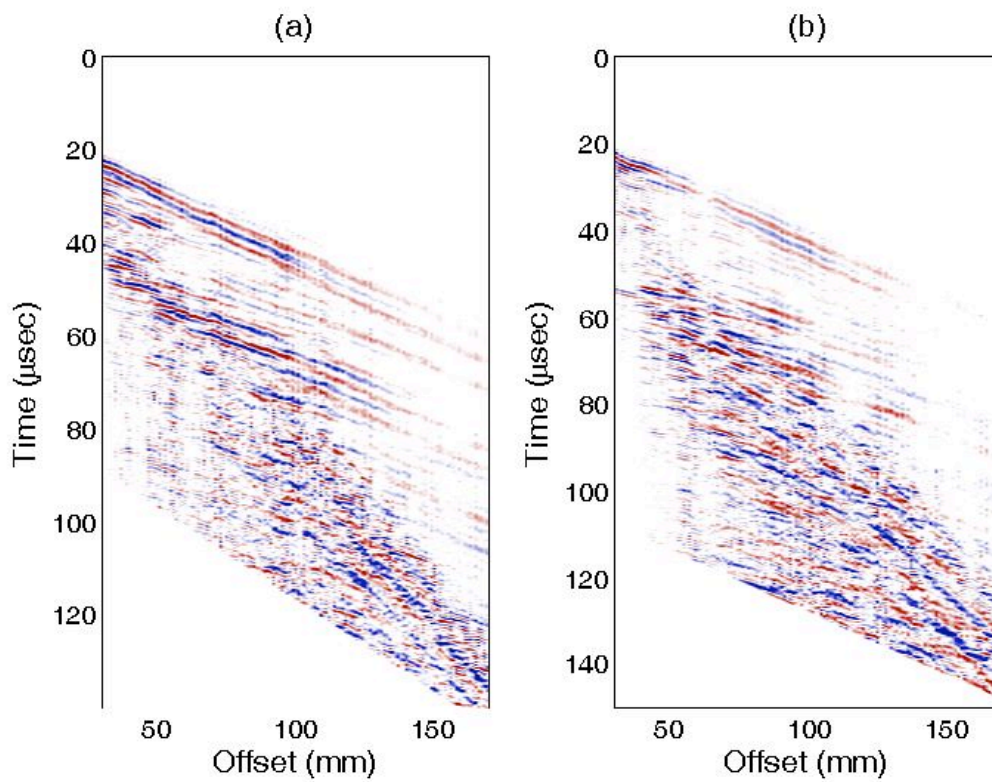


Figure 3.28 The $x - t$ diagrams for (a) human tibia specimen 1 and (b) human tibia specimen 2.

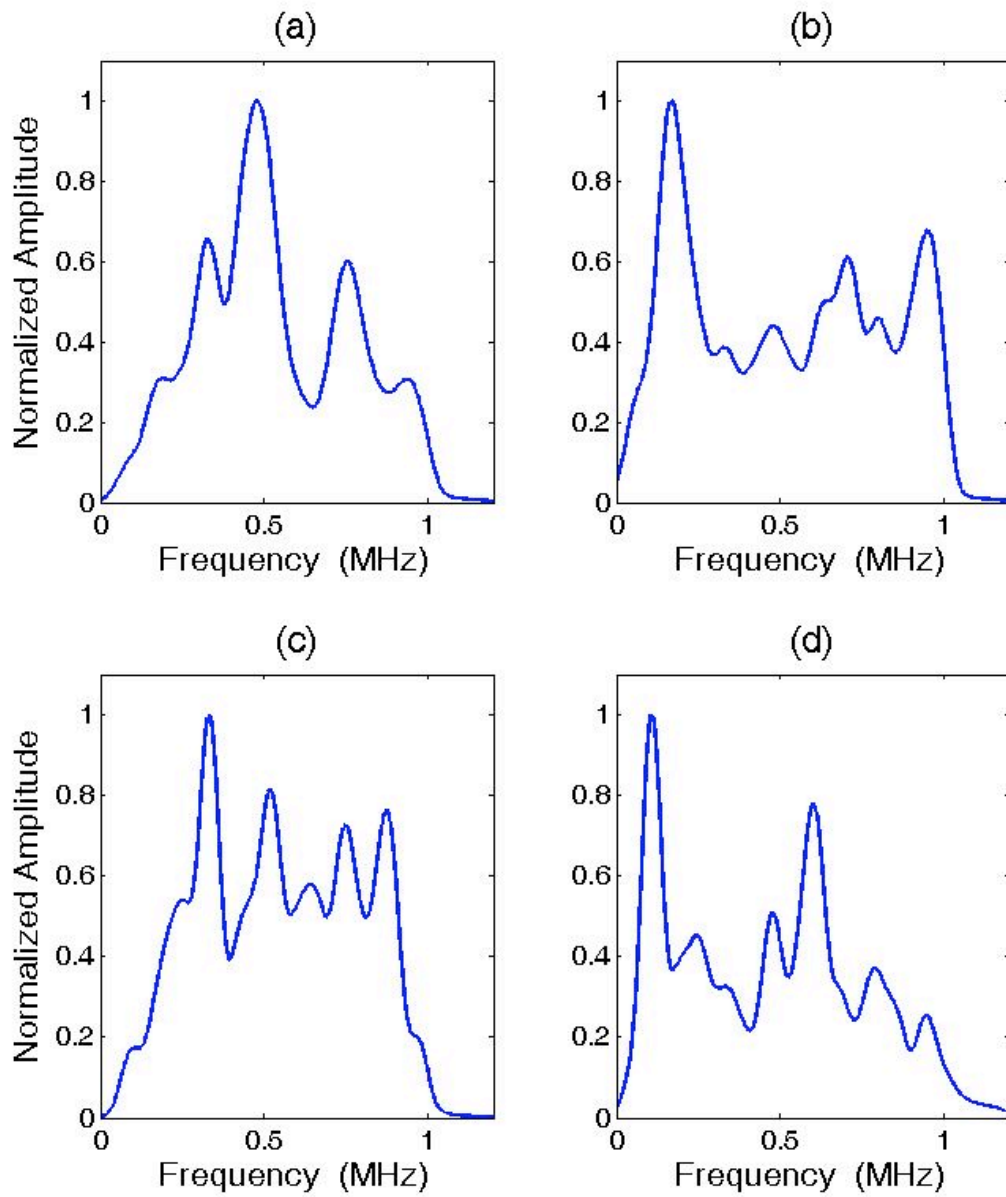


Figure 3.29 The frequency spectra for human tibia specimen 1 at (a) 40 mm, (b) 140 mm and human tibia specimen 2 at (c) 40 mm and (d) 140 mm offsets.

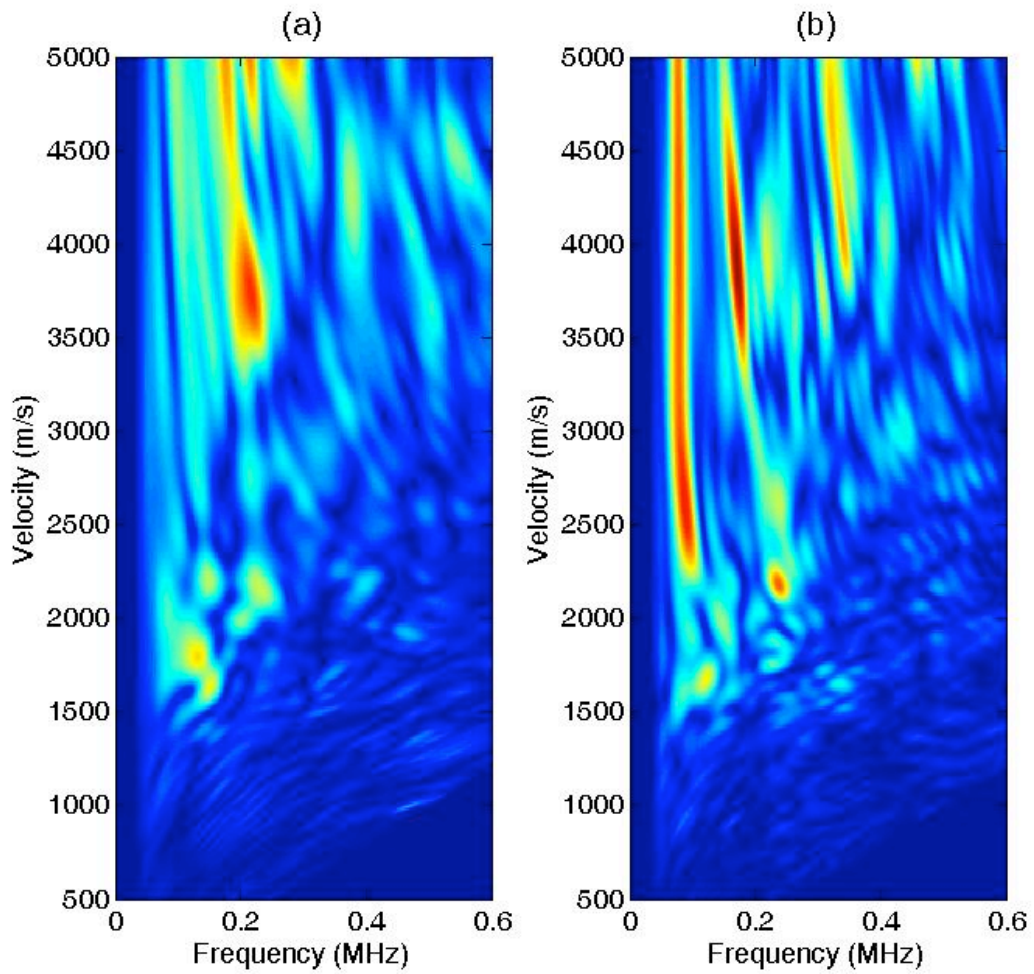


Figure 3.30 The f - c diagrams for human tibiae: (a) specimen 1 and (b) specimen 2.

Chapter 4

Discussion

4.1 Time Domain Data

The time domain data is used to examine the effect of soft tissue on the appearance of the experimental results. There are two basic effects that the soft tissue has on the data. First, the soft tissue modulates the ultrasound signals. At the soft tissue-bone plate interface, some guided wave energy leaks into the soft tissue and reflects back into the bone, changing the propagation of the guided wave (Moilanen et al., 2006). Second, there is a direct compressional wave arrival that travels through the soft tissue with a velocity in the same range as a guided wave in bone. These two effects superimpose to create the overall effect of the soft tissue on the data.

All four experimental data sets show two distinct wave arrivals, the early-arriving body waves and the late-arriving guided waves. These two wave packets have been previously observed by other studies (Nicholson et al., 2002; Lee and Yoon, 2004; Moilanen et al., 2008). The body wave arrival has a similar appearance in all three data sets. This arrival is fast-traveling, high-frequency and is not dispersive. The body wave packet is made up all of the body wave reflections, mode conversions and multiples within the cortical bone layer (Le et al., 2010). The arrival times of the

various embedded phases that make up the body wave arrival are sensitive to small perturbations in shear and compressional wave velocities. These waveforms have been successfully simulated with a simple layer-over-half space model (see Le et al., 2010). The body wave arrival represents the FAS and is consistent with the predicted velocity of a compression arrival in bone ($v_{\text{compressional}} \approx 4000 \text{ m/s}$) (see Figs. 3.1, 3.10, 3.19). In the presence of soft tissue (STBP and HT cases), the first arriving phase is consistent with a lateral compressional wave. The body wave section of the data does not appear to be affected by the presence of soft tissue; the body wave arrivals have the same appearance in all four data sets.

The slow moving wave packet present in the experimental data sets is strongly dispersive and represents the guided wave portion of the data. For finite values of the ratio between wavelength and plate thickness, Lamb waves can undergo dispersion similar to surface waves (Viktorov, 1967; Rose, 1999; Cheeke, 2002). Surface waves are dispersive due to variations in the penetrating depths of different frequency components within vertically stratified layers (Knopoff, 1972; Tatham, 1975; Aki and Richards, 2002; Rapine et al., 2003; Carannante and Boschi, 2005; Boiero and Socco, 2010).

The BP data exhibits a low-frequency guided wave region with a dispersive wave train (Fig. 3.1). In similar experiments, the late-arriving, low-frequency region was found to be consistent with the A_0 mode (Nicholson et al., 2002; Moilanen et al., 2006). Both the STBP and the HT data exhibit a higher frequency guided wave region. At far offset, the lower frequency dispersive wave train was visible in the HT data (Fig.

3.19), but it was not clear in the STBP data. The high-frequency contribution to the data dominates the guided wave portion of the data.

Both the STBP and the BP data resemble the HT data, indicating that the bovine bone plate is a good model for human bones. This further validates our model.

4.2 Frequency Content

The frequency content of the data was examined in three ways: frequency spectra, time-frequency analysis, and frequency-phase velocity mapping.

Frequency Spectra

The frequency spectrum at 40 mm offset looks very similar for all three experiments (see Figs. 3.3a, 3.12a, 3.21a). Each spectrum contains a strong peak at approximately 0.5 MHz as well as some higher frequency energy. The close offset trace exhibits body wave energies only, as guided waves cannot propagate at this short a source-receiver distance. The consistency in the results for the three experiments shows that the body wave regime is not significantly affected by the presence of soft tissue. The body wave signals for the STBP and HT experiments travels through the soft tissue layer, then propagates through the bone, but the signal does not appear to be significantly affected by the soft tissue.

The far-offset traces show a strong, low-frequency maxima from 0.10 – 0.15 MHz. This signal is prominent in all three data sets and does

not appear to be altered by the presence of soft tissue. While the BP data (Fig. 3.3b) has no significant high-frequency contribution at far offset, the two soft tissue cases exhibit a high-frequency contribution at far offset (Figs. 3.12b, 3.21b). This high-frequency signal can be attributed to the presence of soft tissue, either from the compressional wave in soft tissue, or from the soft tissue modulating the guided wave in bone. The direct ultrasound wave through the soft tissue is expected to be a high-frequency contribution, as compressional body waves are higher frequency than guided waves. The high-frequency peaks present in the STBP and HT data sets account for the high-frequency signals in the guided wave portion on the $x - t$ images.

Time – Frequency Analysis

The same high-frequency soft tissue effect seen in the frequency spectra is visible in the $t - f$ results. The spectral decomposition for the BP data (see Fig. 3.4) shows a strong early arriving high-frequency signal that dies out at far offset; this signal is from the body wave arrival and is attenuated at far offset. In the STBP and HT data (see Fig 3.13, 3.22 respectively), the high-frequency contribution persists and arrives at the same times the low-frequency guided waves at far offset. This effect is caused by the soft tissue and this concept is also supported by the frequency spectra discussed above; the high-frequency arrival in the STBP case corresponds to the spectral maxima at 0.7 and 0.8 MHz in the 1D FT data (see Fig. 3.12b).

The low-frequency signal attributed to the guided waves is detected at approximately 0.1 – 0.15 MHz in all three data sets. This is consistent with the low-frequency guided wave detected at the far offset trace in the frequency spectrum.

Frequency –Phase Velocity Mapping

In the BP model, the two fundamental modes A_0 and S_0 were identified. The dominant mode is A_0 , which is visible as the brightest spectral peak at 0.1 MHz (see Fig. 3.8). This mode is noted as being easily detectable (Dodd et al., 2006). The same mode is present as the strong guided wave cluster detected at 0.1 MHz in the frequency spectra (see Fig 3.3) and the $t - f$ map (see Fig 3.4c). The velocity of A_0 is approximately 1200 m/s – 1500 m/s as measured from the $f - c$ map and is within the expected range of guided wave velocities (Nicholson et al., 2002; Moilanen et al., 2006; Moilanen et al., 2007b). This velocity is consistent with the slower wave packet observed in the $x - t$ traces (see Fig 3.1). The same slow wave packet has been observed in other studies and found to be consistent with A_0 (Nicholson et al., 2002; Moilanen et al., 2006). The S_0 mode was also detected. This mode has a higher frequency (0.20 – 0.23 MHz) and a higher velocity (2000 m/s – 3000 m/s) than the A_0 mode. This mode was detected by Moilanen et al. (2006) and they also found it to be weaker than the A_0 mode.

In the presence of soft tissue, guided wave modes change considerably. In the STBP data, more guided wave modes are excited, the energy distribution is altered and the shape of modes is changed. Previous

work into the effect of soft tissue showed that as a layer of soft tissue increases in thickness, the generated modes are more tightly packed together (Moilanen et al 2008). Though our data only examined one thickness of soft tissue, it is clear that the soft tissue proxy resulted in a “denser” mode distribution. Greater mode density has more modes in a smaller frequency range. The STBP data has four guided wave modes excited in the presence of soft tissue: A_0 , S_0 , A_1 , S_1 . Moilanen et al (2006) also found that soft tissue generates more guided wave modes. They were able to generate A_0 in free plates and in an immersed plate experiment, where water was used as a soft tissue mimic. In the immersed plate, they generated A_0 and a bi-layer guided wave mode BL_1 . Their study also indicated that A_0 was not significantly altered by the presence of the water. In our results, the A_0 mode is not significantly changed by the soft tissue mimic.

There is some high-velocity energy present in the $f - c$ space for the STBP that does not correspond to the theoretical modes. This energy cluster is within the range of body wave velocities (3500 m/s – 4000 m/s) and is caused by remnant body wave energy. When the guided waves were isolated with windowing, some body wave energy was still present in the data and is apparent in the $f - c$ image.

Mode identification was not possible for the HT data, as we were unable to generate theoretical dispersion curves for a tube bone model with a soft tissue layer. The $f - c$ of the HT data shows a concentration of two energy areas. The highest energy concentration is higher velocity and represents some body wave energy as well as higher order guided wave

energy. The lower order guided wave energy is seen as the energy peak at the low-frequency, low-velocity area of the $f - c$ map. The spectral energy of the HT data is difficult to interpret, as there is a high degree of noise.

4.3 Numerical Simulation

A numerical simulation was performed to verify the *in vitro* bone plate data. The synthetic data sets for the BP and STBP both exhibited the two wave packets.

The simulated data agrees well with the experimental data and the phases of the real and simulated data are consistent (see Figs. 3.7 and 3.17), validating the synthetic model. The dominant period of the BP guided waves, measured from the figure, is approximately 38% longer than that of the STBP guided waves; this implies that the dominant frequency of the BP guided waves is lower than that of the STBP guided waves, which is supported by the visual appearance of the traces (see Figs. 3.1, 3.10).

Though the simulated traces are lower frequency than the BP and STBP data. The numerical simulation uses infinite, homogenous, isotropic layers to model the experimental data, and these simplifications might lead to the lower frequency in the synthetic data. The experimental work was performed on a bone plate with anisotropies and heterogeneities. The experimental data is higher frequency and includes edge effects from the sides and ends of the plate. In the STBP case, the synthetic exhibits more ringing in the guided wave region of the data than in the experimental

data (see Figs. 3.19, 3.10 respectively); due to the factors mentioned above, the experimental data is more attenuated than the synthetic.

The addition of the simulated data is a key contribution of the numerical modeling. Guided wave modes were successfully generated based on a simplistic, horizontally-layered model. We modeled the bovine tibia plate with two models: the BP (bone-marrow) and STBP (soft tissue-bone-marrow). This work is a great step forward from a previous study focused on synthesizing body wave arrivals in bone (see Le et al., 2010). This effort further validates that the governing principles in seismic waves are consistent with ultrasound wave propagation. The full wavefield calculation performed by the numerical simulation provides an effective method to verify key signals present in the experimental data. Additionally, it sheds insight on the future possibility of accurately quantifying the complex interaction between ultrasonic waves and the bone-soft tissue interface. The first order, layered approximation currently used could have improved accuracy with the addition of more refined 2-D or 3-D structures representing localized defects, velocity heterogeneities, and/or anisotropies. The full-wave form also has the potential for future extractions of bone parameters (velocity, density, attenuation) particularly when based on linearized inversion schemes (see Meneke, 1984; Woo Woodhouse and Dziewonski, 1984).

4.4 Single Value Decomposition

Due to the low signal-to-noise ratio of the human tibia data, an SVD was performed to remove some of the higher frequency noise. This was achieved by performing two SVD operations to separately isolate the guided wave and body wave sections of the data; the high frequency noise was left as a residual of the SVD. The results of these two operations were combined to form the full SVD data set. The $x - t$ data (see Fig. 3.24) showed both wave packets with a lot more clarity. After the SVD, the dispersive wave train in the guided wave packet was more prominent, meaning that the high-frequency signals obscuring the low-frequency wave train were noise. There were some artifacts of the SVD visible in the processed data, including a faint wave that arrives before the FAS at close offset.

The frequency spectra of the SVD results (see Fig. 3.25) greatly resembles the frequency spectra of the BP data (see Fig. 3.3), indicating that the potentially all of high-frequency signals present in guided wave portion of the soft tissue data sets are due to soft tissue signal interference and can be removed with an SVD.

In the $t - f$ data, the high-frequency signal that dominated in the original HT data, is almost entirely eliminated. It is interesting to note that there is still a weak high-frequency signal visible in the far offset $t - f$ that arrives at the same time as the strongest low-frequency guided wave energy (see Figure 3.26c at 110 – 120 μ s) and corresponds to the highest amplitude in the time trace (see Figure 3.26d). This observation lends credence to the idea that most of the high-frequency signal was noise,

while only some was soft tissue signal. This signal is attributed to the presence of the soft tissue, discussed further in the next section.

These observations are continued in the $f - c$ data (Fig. 2.27). With the high-frequency signal filtered out by the SVD, there is considerably less signal present in the image and it is easier to interpret. There are only two main energy clusters present. The $f - c$ has a strong low-frequency component at 0.15 MHz and 1650 m/s. In the BP and STBP data, the strongest signal in the $f - c$ was from the fundamental anti-symmetric mode, A_0 . This mode is consistently low-frequency and low-velocity, which is consistent with the HT mode present in the $f - c$. The A_0 mode is documented as the most prominent guided wave mode (Nicholson et al., 2002), and is most readily detected (Dodd et al., 2006), supporting the idea that the bright mode in the HT data is the A_0 mode. In the BP and STBP data, the A_0 mode had a velocity at approximately 1500 m/s. Though the velocity of this mode is higher than that of the A_0 mode in the *in vitro* data, it is still within the expected range of guided wave velocities for the A_0 mode. As there are not theoretical dispersion curves for the HT data, we are unable to conclusively identify this mode. Additionally, there is some high-frequency content visible in the $f - c$ map. There are two higher order modes visible, one at 0.21 MHz and 3700 m/s and another at 0.15 MHz and 2350 m/s.

The use of the SVD shows that the multiple energy peaks visible in the $f - c$ map for the original HT data do not represent guided wave energy. The SVD filtered $f - c$ map has considerably more focused energy peaks, indicating once again that a lot of the signal present in the rest of

the data was noise. The SVD was highly successful and sheds insight into the nature of the high-frequency signal present in the soft tissue data sets. This study demonstrated that the SVD is successfully able to remove noise from the soft tissue.

4.5 Soft Tissue Complexities

As mentioned earlier, a significant challenge in the study of guided waves is the presence of soft tissue. The direct compressional wave travelling through the soft tissue travels with a velocity that is in the range of guided wave velocities in bone (1300 m/s – 2000 m/s). This makes it possible for the soft tissue signal to be mistaken for guided waves in bone (Moilanen et al., 2006). It has been suggested that line fitting to the wave front can provide an erroneous guided wave velocity, as that velocity is affected by interference with guided wave modes (Moilanen et al., 2006). The soft tissue compressional wave penetrates into the guided wave zone in the $x - t$ data and the interference gives rise to the large amplitude oscillating waveform seen in the STBP data (see Fig. 3.10) and the HT data (see Fig. 3.19).

The frequency content of the soft tissue data sets is very complex. In the BP data, the high-frequency element of the $t - f$ data died out with offset, as the guided wave region became more prominent in the $x - t$ data. In the STBP data, the high-frequency component is visible at all offsets. The high-frequency component in the 140 mm trace arrives at the same time as the low-frequency guided wave signal, and could be

attributed to the compressional wave in soft tissue. The same is shown in the HT data; the high-frequency signal arrives at the same time as the low-frequency guided wave.

The body waves in the BP data set show up as a high-frequency signal on the $t - f$ plot. As the signal in soft tissue is a compressional wave, it would also be expected to be higher frequency. However, this signal dies off as the body wave arrival weakens. The high-frequency signal in the soft tissue data sets persists with offset. In the $t - f$ map, the high-frequency signals in the HT and STBP data sets have the same characteristic appearance as the body wave signal in the BP, adding support to the hypothesis that the high-frequency signals in the soft tissue data are from the compressional wave in soft tissue.

Further support is given to this hypothesis by the SVD processing on the HT data. The SVD removed noise from the data, but the high-frequency signal was still present in the $t - f$ at far offset (Fig. 2.26), indicating that it is not due to noise.

Our understanding of the influence of soft tissue and its affect of the frequency content of the data is incomplete, so we cannot conclude with certainty that this high-frequency signal is due to the compressional wave through the soft tissue. The soft tissue signal is very complex; in addition to the compressional wave through soft tissue, the ultrasound is modified by the presence of soft tissue.

4.6 Reliability and Repeatability

A second human tibia experiment was performed to examine whether the results shown in the human tibia experiment could be repeated on another subject.

The $x - t$ diagrams of the original HT data and the second HT2 data (Fig. 3.28a, b resp.) have a very similar appearance. The HT2 data set shows the same characteristic low-velocity guided and high-velocity body wave packages. Figure 3.28 shows that *in vivo* data of a similar quality was obtained on two different subjects, indicating that the features shown in both data sets are repeatable.

The frequency content of the two human tibia data sets were compared to explore whether similar results could be obtained from multiple *in vivo* experiments. While the frequency content of HT and HT2 are slightly different at close offset, they both illustrate that higher frequencies are dominant at close offset, which is consistent with the *in vitro* experiments as well. The frequency maxima at 40 mm are different in amplitude for the two data sets, but they cover the same frequency range. Frequency maxima are apparent at 0.32 MHz, 0.47 MHz and 0.75 MHz for HT, and 0.32 MHz, 0.52 MHz, 0.74 MHz and 0.87 MHz for HT2. At farther offset, both data sets have a strong low-frequency maximum (0.16 MHz for HT and 0.11 MHz for HT2). The frequency spectra show that the frequency content of the human tibia data is comparable in different human subjects.

The $f - c$ spectrum was also studied for the HT2 data set. Much like the HT $f - c$ map (Fig. 3.30a), the HT2 $f - c$ spectrum (Fig 3.30b) shows a small cluster of low-frequency, low-velocity guided wave energy

that is dominated by low- and high-frequency energies travelling with velocities larger than 2500 m/s.

The results of the HT2 experiment show that *in vivo* data can be successfully obtained in multiple subjects and adds reliability to the HT data results.

Chapter 5

Conclusion and Comments on Further Direction

This thesis aims to explore the way in which soft tissue affects the propagation of ultrasonic guided waves through bone. To this end, we studied the guided wave transmission in a bovine bone plate, the bone plate with a soft tissue mimic, and in a human tibia. We acquired data for the three experiments using the axial transmission method. The data sets were analyzed using frequency spectra, spectral decomposition and frequency-phase velocity mapping. The bovine tibia experiments were augmented with a synthetic simulation, and the $f - c$ spectra results were compared to theoretical dispersion curves. For the *in vivo* human tibia data, a SVD was used to remove noise and enhance lateral coherency of the signals. We were able to look at the change in frequency content in the presence of soft tissue and were able to identify guided wave modes. Experimental results in the bovine bone plate were verified with a synthetic simulation and a comparison to theoretical guided wave modes.

The *in vitro* and *in vivo* ultrasound data exhibit consistently two distinctive wave packets of different velocities: the early-arriving, high-frequency body waves and the late-arriving, low-frequency guided waves. The early-arriving wave packet represents the compressional-type body waves, which attenuate at far offset. The slower wave packet is high-amplitude at far offset and exhibits a dispersive guided wave train. The

presence of soft tissue in the *in vitro* study seems to increase the frequency content of the signal in the guided wave regime. The same phenomenon was also observed in the *in vivo* case. In the *in vitro* data, the shape of guided wave modes changes; mode distribution becomes denser and the energy is spread out more evenly between the modes. The time-frequency analysis demonstrates the cluster of low-frequency guided wave energies around 0.1 – 0.2 MHz, suggesting the optimal excited frequency is around 0.2 MHz, which is also documented in literature. The *in vitro* data agrees well with simulated data. Using dispersive curves, the A_0 and S_0 modes were identified in the BP data at phase velocities 1500 m/s and 2100 m/s respectively. For the STBP data, the A_0 , S_0 , A_1 and S_1 modes were identified at phase velocities 1500 m/s, 1500 m/s, 1900 m/s and 1800 m/s, where the velocity is taken at the maximum amplitude point of each mode.

Research in guided waves in bone is still in its infancy. The bone plate experiments relied on a plate model, which cannot fully explain guided waves in bone. The use of SVD indicates that this technique is a good tool to separate out wave components, and can be applied in further studies. The use of the reflectivity method in developing the synthetic simulation will be of great use in future studies, and can potentially lead to inversions for bone material parameters. This research has great potential in the *in vivo* study of human bone for osteoporosis research and monitoring.

Bibliography

Adler, R. A., 2010, Osteoporosis: Pathophysiology and Clinical Management: Humana Press.

Aki, K. and Richards, P. G., 2002, Quantitative Seismology: University Science Books.

Alleyne, D. and Cawley, P., 1991, A 2-Dimensional Fourier-Transform Method for the Measurement of Propagating Multimode Signals: J. Acoust. Soc. Am., **89**, 1159-1168.

Bartl, R. and Frisch, B., 2009, Osteoporosis: Springer Berlin Heidelberg.

Bilezikian, J. P., Raisz, L. G. and Martin, T. J., 2008, Principles of Bone Biology: Elsevier.

Boiero, D. and Socco, L., 2010, Retrieving lateral variations from surface wave dispersion curves: Geophys. Prospect. **58**, 977-996.

Bonar, D. C. and Sacchi, M. D., 2010, Complex spectral decomposition via inversion strategies: SEG Technical Program Expanded Abstracts, **29**, 1408-1412.

Bonnick, S. L., 2010, Bone Densitometry in Clinical Practice: Application and Interpretation: Humana Press.

Bossy, E., Talmant, M., Defontaine, M., Patat, F. and Laugier, P., 2004, Bidirectional axial transmission can improve accuracy and precision of ultrasonic velocity measurement in cortical bone: a validation on test materials: IEEE Trans. Ultrason. Ferroelectr. Freq. Control, **51**, 71-79.

Bossy, E., Talmant, M. and Laugier, P., 2004, Three-dimensional simulations of ultrasonic axial transmission velocity measurement on cortical bone models: J. Acoust. Soc. Am., **115**, 2314-2324.

- Bossy, E., Talmant, M. and Laugier, P., 2002, Effect of bone cortical thickness on velocity measurements using ultrasonic axial transmission: A 2D simulation study: *J. Acoust. Soc. Am.*, **112**, 297-307.
- Bossy, E., Talmant, M., Peyrin, F., Akrou, L., Cloetens, P. and Laugier, P., 2004, An in vitro study of the ultrasonic axial transmission technique at the radius: 1-MHz velocity measurements are sensitive to both mineralization and intracortical porosity: *J. Bone Miner. Res.*, **19**, 1548-1556.
- Brown, J. P. and Josse, R. G., 2002, Clinical practice guidelines for the diagnosis and management of osteoporosis in Canada: **167**, S1-34.
- Camus, E., Talmant, M., Berger, G. and Laugier, P., 2000, Analysis of the axial transmission technique for the assessment of skeletal status: *J. Acoust. Soc. Am.*, **108**, 3058-3065.
- Carannante, S. and Boschi, L., 2005, Databases of surface wave dispersion: *Ann. Geophys.* **48**, 945-955.
- Cheeke, J. D. N., 2002, *Fundamentals and Applications of Ultrasonic Waves*: Boca Raton: CRC Press.
- Chimenti, D. E., 1997, *Guided Waves in Plates and Their Use in Materials Characterization*: *Appl. Mech. Rev.*, **50**, 247-284.
- Culjat, M., Goldenberg, D., Tewari, P. and Singh, R., 2010, A review of tissue substitutes for ultrasound imaging: *Ultrasound Med. Biol.*, **36**, 861-873.
- Dodd, S. P., Cunningham, J. L., Miles, A. W., Gheduzzi, S. and Humphrey, V. F., 2006, Ultrasonic propagation in cortical bone mimics: *Phys. Med. Biol.*, **51**, 4635-4647.
- Duquette, J., Honeyman, T., Hoffman, A., Ahmadi, S. and Baran, D., 1997, Effect of bovine bone constituents on broadband ultrasound attenuation measurements: *Bone*, **21**, 289-294.

Gerlanc, M., Haddad, D., Hyatt, G. W., Langloh, J. T. and Hilaire, P. S., 1975, Ultrasonic study of normal and fractured bone: *Cli. Orthop. Relat. Res.*, 175-180.

Gilbert, F. and Backus, G., 1966, Propogator matrices in elastic wave and vibration problems: *Geophysics*, **31**, 326-332.

Grampp, S. and Adams, J., 2008, *Radiology of Osteoporosis*: Springer.

Han, S., Rho, J., Medige, J. and Ziv1, I., 1996, Ultrasound velocity and broadband attenuation over a wide range of bone mineral density: *Osteoporosis Int.*, **6**, 291-296.

Haskell, N., 1953, The dispersion of surface waves on multilayered media: *B. Seismol. Soc. Am.* **43**, 17-34.

Joshi, N. R., 2006, Guided Waves, Waveguides and Mode Converted Signals: *Mater. Eval.*, **64**, 337-341.

Kennett, B. L. N., 1983, *Seismic Wave Propagation in Stratified Media*: Cambridge University Press.

Kind, R., 1976, Computation of refelction coefficients for layered media: *J. Geophys.*, **42**, 191-200.

Knopoff, L., 1972, Observation and inversion of surface-wave dispersion: *Technophysics*, **13**, 497-519.

Langton, C. M., Palmer, S. B. and Porter, R. W., 1984, The measurement of broadband ultrasonic attenuation in cancellous bone: *Eng. Med.*, **13**, 89-91.

Langton, C. and Njeh, C., 2008, The measurement of broadband ultrasonic attenuation in cancellous bone - A review of the science and technology: *IEEE T. Ultrason. Ferr.*, **55**, 1546-1554.

Laugier, P., 2006, Quantitative ultrasound of bone: looking ahead: *Joint Bone Spine*, **73**, 125-128.

Laugier, P. and Haiat, G., 2010, *Bone Quantitative Ultrasound*: Springer.

Le, L., Gu, Y., Li, Y. and Zhang, C., 2010, Probing long bones with ultrasonic body waves: *Appl. Phys. Lett.*, **96**.

Lee, K. I. and Yoon, S. W., 2004, Feasibility of bone assessment with leaky Lamb waves, in bone phantoms and a bovine tibia: *J. Acoust. Soc. Am.*, **115**, 3210-3217.

Lefebvre, F., Deblock, Y., Campistron, P., Ahite, D. and Fabre, J. J., 2002, Development of a new ultrasonic technique for bone and biomaterials in vitro characterization: *J. Biomed. Mater. Res.*, **63**, 441-446.

Lowet, G. and Perre, G. V. d., 1996, Ultrasound velocity measurement in long bones: Measurement method and simulation of ultrasound wave propagation: *J. Biomech.*, **29**, 1255-1262.

Marcus, R., 2008, *Osteoporosis*: Elsevier Academic Press.

Menke, W., 1984, *Geophysical Data Analysis: Discrete Inverse Theory*: Academic Press Inc.

Minonzio, J., Talmant, M. and Laugier, P., 2010, Guided wave phase velocity measurement using multi-emitter and multi-receiver arrays in the axial transmission configuration: *J. Acoust. Soc. Am.*, **127**, 2913-2919.

Moilanen, P., Kilappa, V., Nicholson, P., Timonen, J. and Cheng, S., 2004, Thickness sensitivity of ultrasound velocity in long bone phantoms: *Ultrasound Med. Biol.*, **30**, 1517-1521.

Moilanen, P., Nicholson, P. H. F., Kilappa, V., Cheng, S. and Timonen, J., 2006, Measuring guided waves in long bones: Modeling and experiments in free and immersed plates: *Ultrasound Med. Biol.*, **32**, 709-719.

Moilanen, P., 2008, Ultrasonic guided waves in bone: *IEEE Trans. Ultrason. Ferroelectr. Freq. Control*, **55**, 1277-1286.

Moilanen, P., Nicholson, P. H. F., Kilappa, V., Cheng, S. and Timonen, J., 2007a, Assessment of the cortical bone thickness using ultrasonic

guided waves: Modelling and in vitro study: *Ultrasound Med. Biol.*, **33**, 254-262.

Moilanen, P., Talmant, M., Bousson, V., Nicholson, P. H. F., Cheng, S., Timonen, J. and Laugier, P., 2007b, Ultrasonically determined thickness of long cortical bones: Two-dimensional simulations of in vitro experiments: *J. Acoust. Soc. Am.*, **122**, 1818.

Moilanen, P., Talmant, M., Kilappa, V., Nicholson, P., Cheng, S., Timonen, J. and Laugier, P., 2008, Modeling the impact of soft tissue on axial transmission measurements of ultrasonic guided waves in human radius: *J. Acoust. Soc. Am.*, **124**, 2364-2373.

Muller, M., Moilanen, P., Bossy, E., Nicholson, P., Kilappa, V., Timonen, J., Talmant, M., Cheng, S. and Laugier, P., 2005, Comparison of three ultrasonic axial transmission methods for bone assessment: *Ultrasound Med. Biol.*, **31**, 633-642.

Muller, M., Moilanen, P., Talmant, M., Kilappa, V., Nicholson, P., Timonen, J., Cheng, S. and Laugier, P., Axial transmission techniques for bone assessment: an in vitro comparative study, Presented at the Ultrasonics Symposium, 2004 IEEE.

Nicholson, P. H. F., Moilanen, P., Karkkainen, T., Timonen, J. and Cheng, S. L., 2002, Guided ultrasonic waves in long bones: modelling, experiment and in vivo application: *Physiol. Meas.*, **23**, 755-768.

Njeh, C. F., Hans, D., Wu, C., Kantorovich, E., Sister, M., Fuerst, T. and Genant, H. K., 1999, An in vitro investigation of the dependence on sample thickness of the speed of sound along the specimen: *Med. Eng. Phys.*, **21**, 651-659.

Njeh, C., Boivin, C. and Langton, C., 1997, The role of ultrasound in the assessment of osteoporosis: A review: *Osteoporosis Int.*, **7**, 7-22.

Osteoporosis Canada, 2008, Breaking Barriers, Not Bones [electronic Resource]: 2008 National Report Card on Osteoporosis Care: Osteoporosis Canada.

Osteoporosis Canada, Facts and Statistic, <http://www.osteoporosis.ca/>: 2011.

Prevrhal, S., Fuerst, T., Fan, B., Njeh, C., Hans, D., Uffmann, M., Srivastav, S. and Genant, H. K., 2001, Quantitative ultrasound of the tibia depends on both cortical density and thickness: *Osteoporosis Int.*, **12**, 28-34.

Prosser, W., Seale, M. and Smith, B., 1999, Time-frequency analysis of the dispersion of Lamb modes: *J. Acoust. Soc. Am.*, **105**, 2669-2676.

Protopappas, V. C., Fotiadis, D. I. and Malizos, K. N., 2006, Guided ultrasound wave propagation in intact and healing long bones: *Ultrasound Med. Biol.*, **32**, 693-708.

Protopappas, V. C., Kourtis, I. C., Kourtis, L. C., Malizos, K. N., Massalas, C. V. and Fotiadis, D. I., 2007, Three-dimensional finite element modeling of guided ultrasound wave propagation in intact and healing long bones: *J. Acoust. Soc. Am.*, **121**, 3907-3921.

Rapine, R., Tilmann, F., West, M., Ni, J. and Rodgers, A., 2003, Crustal structure of northern and southern Tibet from surface wave dispersion analysis: *J. Geophys. Res.-Solid*, **108**, 11.

Reginster, J. and Burlet, N., 2006, Osteoporosis: A still increasing prevalence: *Bone*, **38**, 4-9.

Rose, J. L., 1999, *Ultrasonic Waves in Solid Media*: Cambridge ; New York : Cambridge University Press.

Ryan, H., 1994, Ricker, Ormsby, Klauder, Butterworth - a choice of wavelets: *CSEG Recorder*, **19**, 8-9.

Siegel, I., Anast, G. and Fields, T., 1958, The determination of fracture healing by measurement of the sound velocity across the fracture side: *Surg. Gynec. Obstet.*, **107**, 327-332.

- Sievänen, H., Cheng, S., Ollikainen, S. and Uusi-Rasi, K., 2001, Ultrasound Velocity and Cortical Bone Characteristics In Vivo: Osteoporosis Int., **12**, 399-405.
- Spitz, S., 1991, Seismic trace interpolation in the F-X domain: Geophysics, **56**, 785-794.
- Ta, D., Huang, K., Wang, W., Wang, Y. and Le, L. H., 2006, Identification and analysis of multimode guided waves in tibia cortical bone: Ultrasonics, **44**, E279-E284.
- Ta, D., Wang, W., Wang, Y., Le, L. H. and Zhou, Y., 2009, Measurement of the Dispersion and Attenuation of Cylindrical Ultrasonic Guided Waves in Long Bone: Ultrasound Med. Biol., **35**, 641-652.
- Tatarinov, A., Sarvazyan, N. and Sarvazyan, A., 2005, Use of multiple acoustic wave modes for assessment of long bones: Model study: Ultrasonics, **43**, 672-680.
- Tatham, R., 1975, Surface-wave dispersion applied to detection of sedimentary basins: Geophysics, **40**, 40-55.
- Thomson, W. T., 1950, Transmission of Elastic Waves through a Stratified Solid Medium: J. Appl. Phys., **21**, 89-93.
- Tortora, G. J. and Grabowski, S. R., 2003, Principles of Anatomy and Physiology: Wiley.
- Turner, C. H., 2002, Biomechanics of bone: determinants of skeletal fragility and bone quality: Osteoporosis Int., **13**, 97-104.
- Vavva, M. G., Protopappas, V. C., Gergidis, L. N., Charalambopoulos, A., Fotiadis, D. I. and Polyzos, D., 2008, The effect of boundary conditions on guided wave propagation in two-dimensional models of healing bone: Ultrasonics, **48**, 598-606.
- Verhoef, W. A., Cloostermans, M. J. and Thijssen, J. M., 1985, Diffraction and dispersion effects on the estimation of ultrasound attenuation and velocity in biological tissues: IEEE T. Bio-Med. Eng. **32**, 521-529.

Viktorov, I. A., 1967, Rayleigh and Lamb Waves: New York, Plenum Press.

Werner, P., 2004, Knowledge about osteoporosis: assessment, correlates and outcomes: *Osteoporosis Int.*, **16**, 115-127.

Woodhouse, J. H. and Dziewonski, A. M., 1984, Mapping the Upper Mantle: Three-Dimensional Modeling of Earth Structure by Inversion of Seismic Waveforms: *J. Geophys. Res.*, **89**, 5953-5986.

Zhao, B. B. and Chen, Y. Q., 2011, Singular value decomposition (SVD) for extraction of gravity anomaly associated with gold mineralization in Tongshi gold field, Western Shandong Uplifted Block, Eastern China: *Nonlinear Proc. Geoph.*, **18**, 103-109.

Appendix A

Guided Wave Propagation in a Free Plate

The two-dimensional wave equations for the displacement potentials, ϕ and ψ are

$$\frac{\partial^2 \phi}{\partial x^2} + \frac{\partial^2 \phi}{\partial z^2} = \frac{1}{c_L^2} \frac{\partial^2 \phi}{\partial t^2} \quad (\text{A.1})$$

for longitudinal waves and

$$\frac{\partial^2 \psi}{\partial x^2} + \frac{\partial^2 \psi}{\partial z^2} = \frac{1}{c_T^2} \frac{\partial^2 \psi}{\partial t^2} \quad (\text{A.2})$$

for shear waves where the c_T and c_L are the longitudinal and transverse velocities given by

$$c_L^2 = \sqrt{\frac{\lambda + 2\mu}{\rho}} \quad \text{and} \quad c_T^2 = \sqrt{\frac{\mu}{\rho}} \quad , \quad (\text{A.3})$$

where ρ is density. The terms λ and μ are the Lamé constants.

The displacement vector, $\mathbf{U} = (u, w)$, and the potentials are related by

$$u = \frac{\partial \phi}{\partial x} + \frac{\partial \psi}{\partial z}, \quad (\text{A.4})$$

$$w = \frac{\partial \phi}{\partial z} + \frac{\partial \psi}{\partial x}. \quad (\text{A.5})$$

The stress components can be expressed in the form

$$\begin{aligned} \sigma_{zx} = \sigma_{xz} &= \mu \left(\frac{\partial w}{\partial x} + \frac{\partial u}{\partial z} \right) \\ &= \mu \left(\frac{\partial^2 \phi}{\partial x \partial z} - \frac{\partial^2 \psi}{\partial x^2} + \frac{\partial^2 \psi}{\partial z^2} \right), \end{aligned} \quad (\text{A.6})$$

and

$$\begin{aligned} \sigma_{zz} &= \lambda \left(\frac{\partial u}{\partial x} + \frac{\partial w}{\partial z} \right) + 2\mu \frac{\partial w}{\partial z} \\ &= \lambda \left(\frac{\partial^2 \phi}{\partial x^2} + \frac{\partial^2 \phi}{\partial z^2} \right) + 2\mu \left(\frac{\partial^2 \phi}{\partial z^2} - \frac{\partial^2 \psi}{\partial z \partial x} \right). \end{aligned} \quad (\text{A.7})$$

Following Rose (1999), we assume the solutions to (A.1) and (A.2) take the following form:

$$\phi(x, z, t) = [A_1 \sin(\rho z) + A_2 \cos(\rho z)] \exp[i(kx - \omega t)], \quad (\text{A.8})$$

$$\psi(x, z, t) = [B_1 \sin(qz) + B_2 \cos(qz)] \exp[i(kx - \omega t)]. \quad (\text{A.9})$$

These solutions represent waves travelling in the x direction and standing waves in the z direction. The variables A_1 , A_2 , B_1 and B_2 are unknown constants. The vertical wavenumbers, p and q are defined as

$$p^2 = \frac{\omega^2}{c_L^2} - k^2 \text{ and } q^2 = \frac{\omega^2}{c_T^2} - k^2 \quad (\text{A.10})$$

where k is the wavenumber.

By substituting (A.8) and (A.9) into (A.4) and (A.5) and omitting the harmonic term $\exp[i(kx - \omega t)]$, we obtain the stress components as

$$\begin{aligned} \sigma_{zx} = & 2i\mu kp[A_1 \cos(pz) - A_2 \sin(pz)] \\ & + (k^2 - q^2)[B_1 \sin(qz) + B_2 \cos(qz)], \end{aligned} \quad (\text{A.11})$$

$$\begin{aligned} \sigma_{zz} = & -\lambda(k^2 + p^2)[A_1 \sin(pz) + A_2 \cos(pz)] \\ & - 2\mu p^2[A_1 \sin(pz) + A_2 \cos(pz)] \\ & - 2i\mu kq[B_1 \cos(qz) - B_2 \sin(qz)]. \end{aligned} \quad (\text{A.12})$$

Following Rose (1999), the solutions can be split into symmetric and anti-symmetric modes. This is possible as sines are odd functions about the $z = 0$ axis and cosines are even about the $z = 0$ axis. The symmetric modes are defined by the following equations

$$\begin{aligned} \phi &= A_2 \cos(pz), \\ \psi &= B_1 \sin(qz), \\ u &= ikA_2 \cos(pz) + qB_1 \cos(qz), \\ w &= -pA_2 \sin(pz) - ikB_1 \sin(qz), \\ \sigma_{zx} &= \mu [-2ikpA_2 \sin(pz) + (k^2 - q^2) B_1 \sin(qz)], \\ \sigma_{zz} &= -\lambda(k^2 + p^2)A_2 \cos(pz), \\ & - 2\mu [p^2 A_2 \cos(pz) + ikqB_1 \cos(qz)] \end{aligned} \quad (\text{A.13})$$

For the symmetric modes, the wave structure is symmetric across the plate for u and anti-symmetric for w . The unknown constants A_2 and B_1 can be determined by applying the stress-free boundary conditions at $z = h$, half the plate width, i.e.,

$$\begin{bmatrix} -2i\mu k p \sin(\rho h) & \mu(k^2 - q^2) \sin(qh) \\ -(\lambda k^2 + \lambda \rho^2 + 2\mu \rho^2) \cos(\rho h) & -2i\mu k q \cos(qh) \end{bmatrix} \begin{bmatrix} A_2 \\ B_1 \end{bmatrix} = 0. \quad (\text{A.14})$$

In order to find non-zero solutions of this matrix, it is required that the determinant is zero, which gives us the following equation

$$\frac{(k^2 - q^2) \sin(qh)}{2i\mu k p \sin(\rho h)} = \frac{-2i\mu k q \cos(qh)}{(\lambda k^2 + \lambda \rho^2 + 2\mu \rho^2) \cos(\rho h)}. \quad (\text{A.15})$$

With some manipulation, this can be rewritten as

$$\frac{\tan(qh)}{\tan(\rho h)} = \frac{4k^2 q \rho \mu}{(\lambda k^2 + \lambda \rho^2 + 2\mu \rho^2)(k^2 - q^2)}. \quad (\text{A.16})$$

In terms of (A.3), we write

$$\lambda = c_L^2 \rho - 2\mu \text{ and } c_T^2 = \mu / \rho. \quad (\text{A.17})$$

Using (A.17) the denominator in the right side of equation (A.16) can be re-written as

$$\begin{aligned}
\lambda k^2 + \lambda p^2 + 2\mu p^2 &= \lambda(k^2 + p^2) + 2\mu p^2 \\
&= (c_L^2 \rho - 2\mu)(k^2 + p^2) + 2\mu p^2 \\
&= c_L^2 \rho(k^2 + p^2) + -2\mu k^2 .
\end{aligned} \tag{A.18}$$

Using (A.10) and (A.18) we can get

$$\begin{aligned}
\lambda k^2 + \lambda p^2 + 2\mu p^2 &= \rho \omega^2 - 2\rho c_T^2 k^2 \\
&= \rho c_T^2 \left[\frac{\omega^2}{c_T^2} - 2k^2 \right] \\
&= \rho c_T^2 (q^2 - k^2) \\
&= \mu (q^2 - k^2)
\end{aligned} \tag{A.19}$$

Substituting this result back into (A.16) gives us the dispersion equation for the symmetric modes,

$$\frac{\tan(qh)}{\tan(ph)} = -\frac{4k^2 qp}{(q^2 - k^2)^2} \tag{A.20}$$

Similarly, the anti-symmetric modes are governed by the following equations

$$\begin{aligned}
\phi &= A_1 \sin(pz), \\
\psi &= B_2 \cos(qz), \\
u &= ikA_1 \sin(pz) - qB_2 \sin(qz), \\
w &= pA_1 \cos(pz) - ikB_2 \cos(qz), \\
\sigma_{zx} &= \mu [2ikpA_1 \cos(pz) + (k^2 - q^2) B_2 \cos(qz)], \\
\sigma_{zz} &= -\lambda (k^2 + p^2) A_1 \sin(pz) \\
&\quad - 2\mu [p^2 A_1 \sin(pz) + ikqB_2 \sin(qz)].
\end{aligned} \tag{A.21}$$

Following the same procedure outlined for the symmetric modes, the dispersion equation for the anti-symmetric modes can be written as

$$\frac{\tan(qh)}{\tan(ph)} = -\frac{4k^2 qp}{(q^2 - k^2)^2}. \tag{A.22}$$